prepared at room temperature [139]. On the other hand, our measurements clearly exclude the formation of a sharp interface between the Fe film and the Si or Ge substrate. Also the idea of one alloy in the spacer independent of the overlayer thickness [140] or a composition gradient at the interfaces [141] must be ruled out.

In conclusion, we have shown that the spacer layers of the trilayers prepared at low temperatures by Toscano et al. [137] and Walser et al. [95] are indeed pure amorphous semiconductors. The thickness dependence, however, has to be recalibrated because we find evidence for interdiffusion at the Fe/Ge as well as the Fe/Si interface. Silicon (germanium) deposited on Fe, on the other hand, does not react within the resolution of our experiment. Therefore, in the case of Si the spacer layer thickness is reduced by $\approx \delta = 10$ Å compared to nominal spacer thickness. The δ is the amount of semiconductor material that interdiffuses into the Fe top layer. In addition, we have shown by investigating the chemical shifts of the core level peaks that the thickness of the interdiffused layer depends on the substrate temperature. This might be one reason for the quite distinct magnetic results obtained from Fe/Si/Fe layers that have been prepared at different temperatures. However, while the chemical shifts of the corresponding core level peaks for layers prepared at 40 and at 290 K, respectively, differ considerably, the difference in the amount of interdiffused material as obtained by inelastic background analysis is rather small. The question as to how the differences in magnetic behavior between the different systems can be explained still remains unanswered.

5 SCANNING PROBE MICROSCOPY

Deeper understanding of the relation between function and structure requires linking observed physical properties directly to the geometric atomic structures. Diffraction methods (see Section 3) can yield very precise information on the crystallography of surfaces and solids, but nonperiodic, very complex surface structures are in general not accessible by such methods. Scanning probe microscopy (SPM) techniques are the methods of choice here. A starting point was the scanning tunneling microscope, which allows measurement of the topography of surfaces with very good resolution up to subatomic features. Methodical spin-offs provide maps of various physical properties on a very local scale (up to Å).

PART III. SCANNING TUNNELING MICROSCOPY

Scanning tunneling microscopy (STM) has become an extremely powerful method for surface topography and structure. This was the first technique capable of atomic resolution on flat surfaces. The first atomically resolved images of the (7 × 7) structure of Si(111) were published in 1982 [142]. In 1986 the Nobel price for physics was awarded to Binnig and Rohrer for the development of the STM method together with Ruska for the development of the electron microscopy method.

5.1 Method

For STM, both electrodes, the probe and the sample, must be conductive. A sharp tip is used as a probe, and it is usually produced by electrochemical etching of a tungsten wire in KOH or NaOH solution (see Section 5.1.1). The tip is brought close to the sample surface by piezoelements until a tunnel current in the nA-range flows through the vacuum or air gap.

A gap in between two conductive materials represents an energetic barrier for electron waves. In the media the wave can propagate quasifreely and in the barrier it is damped exponentially with the penetration depth,

$$I \propto e^{-2\kappa d} \quad \text{with} \quad \kappa = \sqrt{2m\bar{\Phi}}/\hbar \qquad (47)$$

m is the electron mass, d is the spatial gap width, and $\bar{\Phi}$ is the energetic barrier height, which is related to the mean work function of both electrode materials. Compared with free surfaces the work functions of proximate electrodes are lowered significantly due to the image charge.

The maximal possible current flowing through an atomically sharp tip is of the order $I_0 = U/R_K$ with gap voltage U and Klitzing constant $R_K = h/e^2 \approx 25$ kΩ. Actual tunnel currents are of the order 1 nA. The saturation of preamplifiers used in STM is typically reached with 50 nA.

For steady electron tunneling conditions a small bias U must be applied between sample and tip. A tunnel current of a few nA indicates that the distance between probe and sample is of the order of some 10 Å, that is, typical wave lengths of the valence and conduction electrons close to the Fermi level. With crystalline materials the wave lengths of the electrons contributing to the tunnel current depend on the effective mass m^* and on the relative energy with respect to the bottom of the bulk or surface band E_0 from which the tunnel electrons originate:

$$\lambda_{\text{de Broglie}} = \frac{h}{\sqrt{2m^*(E - E_0)}} \qquad (48)$$

As the amplitude of the electron wave is exponentially damped in the gap the tunneling current is an extremely sensitive measure of the changes of distance [143]. This high sensitivity is vital in STM.

After the approach of the probe to the sample a regulation loop of the current is activated, that adjusts the z fine piezoelement according to the feedback set-

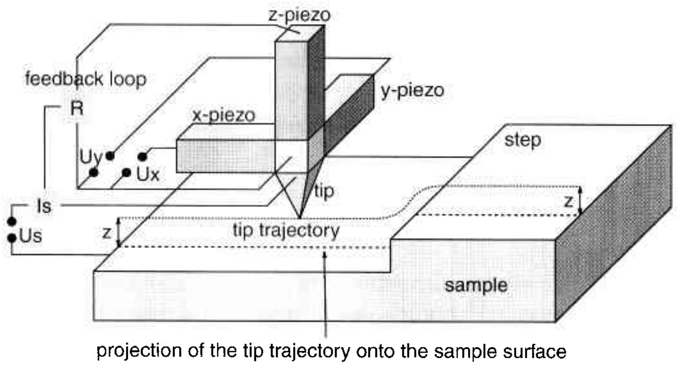

FIG. 43. Illustration of the working principle of the STM method.

point current. The tip scans a point lattice on the surface by moving the x and y piezoelements stepwise. The z piezovoltages necessary to keep the tunnel current constant are taken in a data set and give a height map of the surface $z(x, y)$ (Fig. 43). When the tip is sharp and clean and the surface is flat and clean, atomic resolution is easily obtained because generally more (or less) electrons are accessible above the surface atoms than in between them. Thus, regulation retracts or lowers the tip according to the atomic structure. In this so-called constant current mode (CCM) the current (i.e., constant *microscopic* distance) is kept constant and changes in height of the tip are measured. This is the most commonly used mode. The measured height maps are actually a surface of constant surface density of states ($\rho_{\text{sample}}(r_{\text{tip}}, E)\rho_{\text{tip}}(E - eU) \overset{!}{=}$ constant). The z signal is the result of both the geometrical and electronic properties of the sample surface. With higher gap voltages U, it is necessary to realize that the *integrated and weighted* charge density between the Fermi level E_F and the energy of the applied gap voltage eU enter in the tunnel current.

$$I \propto \int_{E_F}^{E_F+eU} dE\ \rho_{\text{sample}}(r_{\text{tip}}, E)T(E, U) \tag{49}$$

here $T(E, U)$ is the transmission coefficient. This formula neglects the variation of the density of states of the tip. With metallic samples the measured map of z-piezo heights corresponds roughly to an envelope of the atoms in the surface. With semiconducting samples the electrons are less delocalized and the density of states (DOS) is more structured, hence STM "topography" is afflicted to a larger extent with electronic effects and is energy dependent (eU).

A different, much faster mode is with regulation switched off or slowed down. Then the height, that is, the z piezolength, stays constant while scanning. The tunneling current, that is, also the local tip-surface distance, changes with x and y and

is recorded. The disadvantage of this constant height mode (CHM) is that it only gives a qualitative image of the surface topography, which means no exact heights are obtained. Actually, this mode measures the regulation error that behaves qualitatively like the differentiation of the topography. The edges of geometrical and electronical features are emphasized in such images.

Today low-temperature STMs at liquid He temperature, variable-temperature STMs offering cooling and annealing, high-speed-STMs allowing movie shots, and liquid-phase STMs for the study of electrolytic surface reactions have been developed and are commercially available.

5.1.1 Probes. Most commonly used are tungsten probes that have been electrochemically etched in KOH or NaOH solution. For example, a 0.4-mm thick tungsten wire, initially annealed, can be used as an anode and a copper wire of equal thickness can be used as a cathode. The etching can be done in 2N KOH solution, with 16 V DC voltage and a decreasing current of $\approx 20 \ldots 3$ mA. With some conditions, for example, for tunneling on H_2O films, problems arise with tungsten tips. The PtIr tips are an alternative. They can be either etched or just cut off by a pair of pliers.

With flat surfaces a mesoscopically blunt tip can yield atomic resolution because minitips form after treatment with voltage pulses up to 10 V during tunneling. The most protruding minitip is the active tunneling area. The rougher the sample the more probable are artifacts because the tip contacts larger objects sideways and the active tunnel region changes occasionally during the scan. Thereby higher objects can be imaged multiply in larger frames (ghost images) or steps on single crystal surfaces can be imaged with heights that correspond to fractions of the interlayer spacing.

5.2 Topographies

In view of the huge number of surface systems that have been successfully studied by STM we give in the following section examples for the different categories of systems. It must be mentioned that the interpretation of STM images can become difficult or even impossible unless other standard surface analytical tools, such as LEED/RHEED (Section 3.2), AES (Section 4.3), or LEIS (Section 2.2) are employed.

5.2.1 Clean, Low-Indexed Surfaces. The structures of clean surfaces are of fundamental interest because they are the basis for more complicated systems offering practical applications. On their own, clean surfaces have importance as quasi-2D systems, which can show special effects like relaxations, reconstructions, phase transitions, surface-specific defects, local mass fluctuations, and roughening transitions. In the following we concentrate on face-centered cubic (fcc) metals. The geometry of the three low-indexed fcc surfaces is shown in Figure 44.

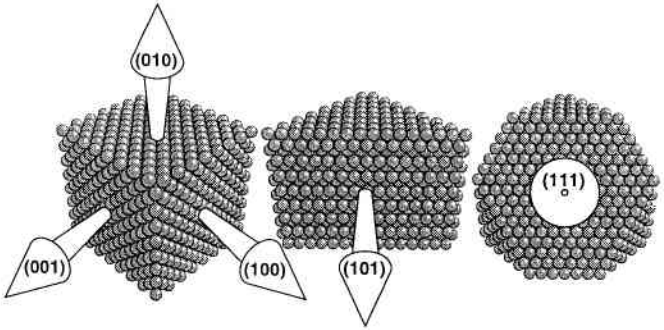

FIG. 44. Sphere models of the three low-indexed planes of the face-centered-cubic-crystal structure.

The equilibrium structure of many clean surfaces has been cleared up or corroborated by the help of STM. Early findings were the missing row reconstructions on Au(110) [144, 145] and Pt(110) [146, 147]. These reconstructions exist together with a mesoscopic step net structure called fishscale pattern [147, 148]. This structure could be detected only by STM and not by standard crystallographic methods such as LEED. The origin of the reconstruction is the higher energy of the {111} microfacets. The fishscale pattern serves to hide antiphase domain walls in order to keep the surface energy high. The surface energy is defined as the excess free energy per unit area [149]. On fcc(110) surfaces the fishscale pattern is never present with reconstructions other than (1 × 2), for example, with the (1 × 4) reconstruction of Pt(110) [150].

A remarkable exception was the Ir(110) surface. Its equilibrium structure is a mesoscopically corrugated hill-and-valley structure with {331} facets exposed, 13.3° inclined with respect to (110) (Fig. 45) [151]. Up-and-down sequences of these facets show a period of 10–100 Å (Fig. 45). Additionally, a mesoscopic waviness with periods of approximately 1000 Å is observed. With certain adsorbates, for example, oxygen, an unreconstructed surface with large terraces instead of the hill-and-valley structure can be prepared and atomically resolved [152]. At elevated temperatures a (1×2) reconstruction is obtained [153]. To date there is no calculation for the faceted structure of Ir(110) and its origin is unexplained. One may argue that such structures are surface stress induced, as was evoked with the corrugated iron structure of Pt(110), which is observed on a very large scale, exhibiting periods of ≈1500 Å [154].

5.2.2 Stepped Surfaces. Steps on vicinal surfaces are interesting because they represent a set of one-dimensional (1D) nanostructures. A regular step array is most often observed [155–158] though at low temperatures the energetic minimum can be a faceted surface [159]. The origin of this order is the step-step repulsion. In a simple approach the step-step interaction can be divided into three contributions: entropic; electronic; and elastic interaction.

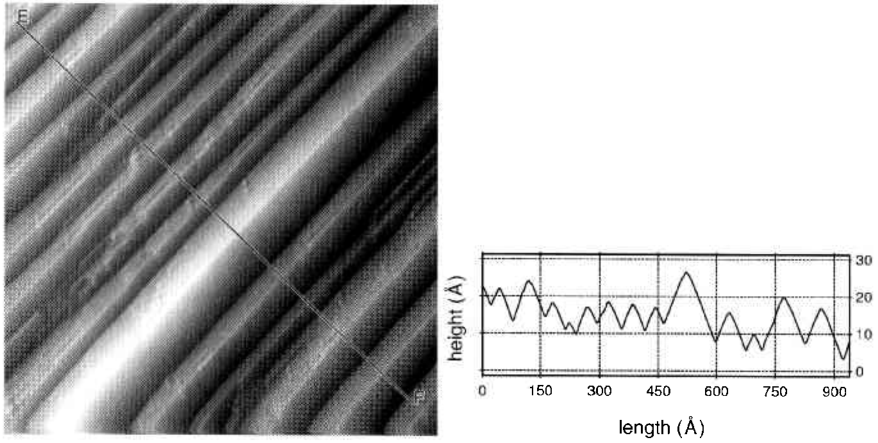

FIG. 45. The STM image of Ir(110) after standard preparation (a) and line section between points E and F. (b) 770 Å, −0.9 V, 1.0 nA. The structure consists of up- and-down sequences of {331} facets inclined by 13.3° [152]. Reprinted with permission J. Kuntze (doctoral dissertation).

Elastic interaction occurs when the displacement fields from steps substantially superpose. Atoms located in the vicinity of steps tend to relax stronger compared to those farther away. The resulting displacements or lattice distortions decay with increasing distance perpendicular to the steps. Atoms situated in between two steps experience two opposite forces and cannot fully relax to an energetically more favorable position as would be the case with quasiisolated steps. The line dipoles at steps are due to Smoluchowski smoothing [160] and interact electronically. Only dipole components perpendicular to the vicinal surface lead to repulsion whereas parallel components would lead to attractive interaction. The dipole-dipole interaction seems to be weaker than the elastic one. For instance, steps on vicinal Ag(111) have weak dipoles as was shown in a theoretical study [161]. Entropic interaction is due to the condition that steps may not cross and leads to an effective repulsive potential, the weakest interaction type. This contribution is always present and results from the assumption that cavities under the surface are unstable. Experiments and theory investigating steps on surfaces were recently reviewed [162].

Surfaces vicinal to fcc(111) and the miscut about the $\langle\bar{1}\bar{1}2\rangle$ direction, that is, with steps running along the dense $\langle\bar{1}10\rangle$ direction, still can differ. Due to ABC stacking, the fcc $\{11\bar{2}\}$ planes are not mirror planes and the minifacets at the steps

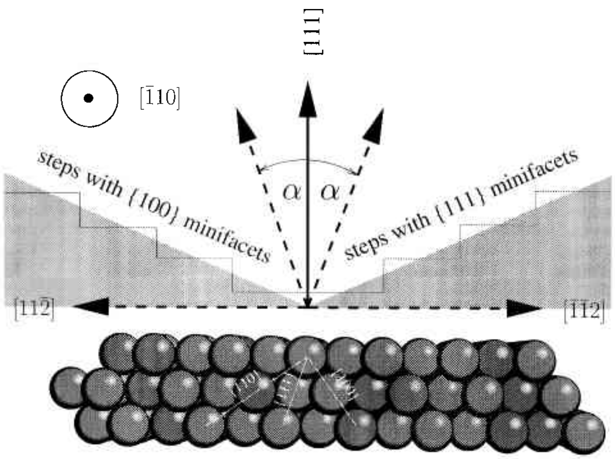

FIG. 46. Side view of a fcc(111) sphere model, illustrating the fabrication of pairs of vicinal surfaces with equal miscut but different minifacet orientation.

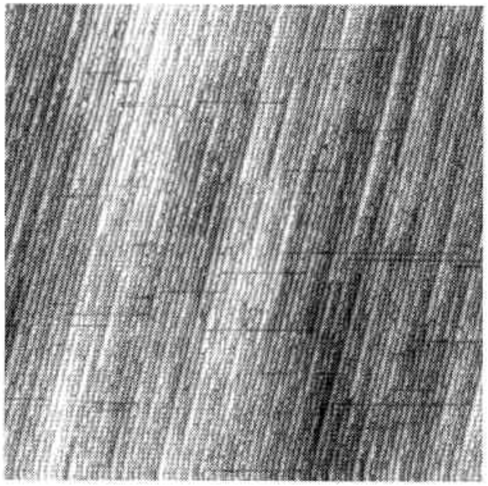

FIG. 47. ⟨110⟩ steps with closed minifacets on a Cu(111) surface with 11° miscut angle; 1000 Å, −1.4 V, 0.5 nA [164]. (Unpublished work by A. R. Bachmann et al.)

are either of {100} or {111} type, depending on whether the miscut is clockwise or counterclockwise (Fig. 46).

Figure 47 shows STM images of the 11° miscut samples with {111} minifacets. The parallel steps run from top to bottom. The upward direction of the steps is from right to left. Regular patterns of monoatomic steps as shown in Figure 47 have been observed on surfaces with {100} and {111} step types and with 5°, 7°, 9°, and 11° miscuts [163]. In STM images the step edges exhibit so-called frizziness, which indicates that atoms move along step edges and that the STM under-samples the topography in time. At room temperature this is a typical feature of materials with relatively low binding energy (e.g., Pb, Ag, and Cu). The frizziness at the {111} steps was found to be stronger than with {100} steps on the 9° miscut surfaces [164].

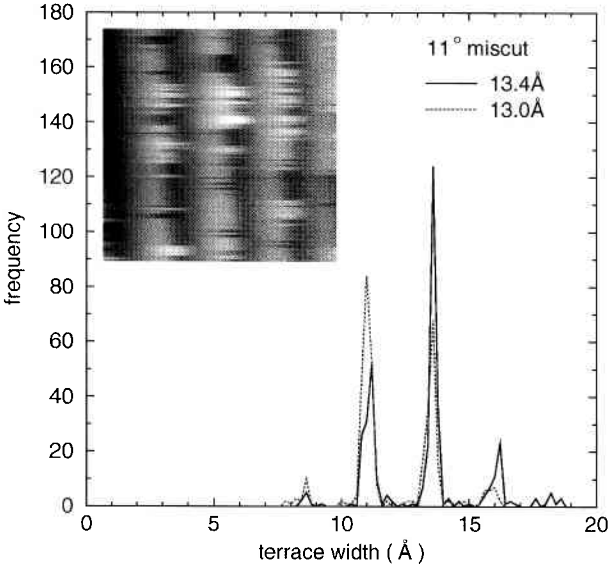

FIG. 48. Terrace width distribution histogram of ⟨110⟩ steps on 11° miscut surface. The inset shows a small frame of 50 Å, −1.4 V, 0.5 nA [164]. (Unpublished work by A. R. Bachmann et al.)

Figure 48 shows a histogram of the terrace widths calculated from the STM frame shown in the inset. The maxima of the terrace width distributions are separated by $a_\perp = 2.2$ Å. Thus, one may conclude that step edge atoms spend the predominant part of time in fcc compatible hollow sites, indicating that their jump rate is moderate compared to the sampling rate (here 2.5 kHz). With lower miscuts, that is, wider terraces, quantization is less pronounced. Analyses of terrace width distributions and of step correlation functions, extracted from STM frames, allow the determination of the step-step interaction potential and the dimensionality of the diffusion processes at steps [165, and references therein].

5.2.3 Alloy Surfaces. Alloy surfaces are important for catalysis. For instance, Pt_3Sn surfaces catalyse many dehydrogenation reactions better than pure Pt. Further motivation can be material economization, for example, the dilution of pure Au with Pd without loss of desired properties such as chemical inertness. With respect to nanostructuring, the wider spectrum of preparable surface structures is of importance. Due to the stress in the surface region highly specific self-ordering structures, like strain relief patterns or faceting, can be prepared.

With alloy surfaces the phenomena of preferential sputtering and segregation govern equilibrium and metastable structures. The component with lighter atoms is most often preferentially sputtered and hence depleted in the surface region. In a first approximation, the component that has the lower surface energy as pure material will segregate because this will enhance surface energy. As a rough estimate, one may compare the melting temperatures of the pure materials instead of the surface energies. A segregation database for transition metals based on LMTO calculations is given Reference [166]. Restoring the original composition in the surface region after sputtering requires a higher temperature than annealing of the geometrical sputter damages because the first requires bulk diffusion and the latter only surface diffusion.

Two principal categories of alloys can be distinguished with binary alloys A_xB_{1-x}. The component that is less efficiently sputtered segregates towards the surface. For instance, with Au_3Pd surfaces the Pd is more efficiently sputtered and Au segregates ($m_{Pd} < m_{Au}$ and $T_{Pd} > T_{Au}$). The Au_3Pd crystallizes in the fcc structure without strict chemical order. Standard preparation leads to a pure unreconstructed Au(100) layer on the alloy with the lattice constant of $a_{Au_3Pd} = 3.99$ Å [46]. An unreconstructed Au layer is special because pure low indexed Au surfaces on Au ($a_{Au} = 4.08$ Å) always reconstruct in equilibrium. In the Au(100) quasihexagonal (5 × 1) reconstruction [167, 168] the surface atoms are compressed with respect to the bulk. One can argue that the $Au_3Pd(100)$ surface provides a substrate that allows a stress-free Au(100) layer (Fig. 49).

A flat Au_3Pd surface with nonzero Pd concentration in the first layer can be prepared when there is sputtering when the crystal is being annealed. The Pd atoms show up in the low energy ion scattering (LEIS) (see Section 2.2) signal and by chemical contrast in STM [46]. They are measured as protrusions with larger apparent STM height than the Au atoms. There was no indication for chemical order in the alloy surface observed. Only the vertical composition profile of the outermost three layers shows slight oscillations as shown in a $I(V)$-LEED study [169].

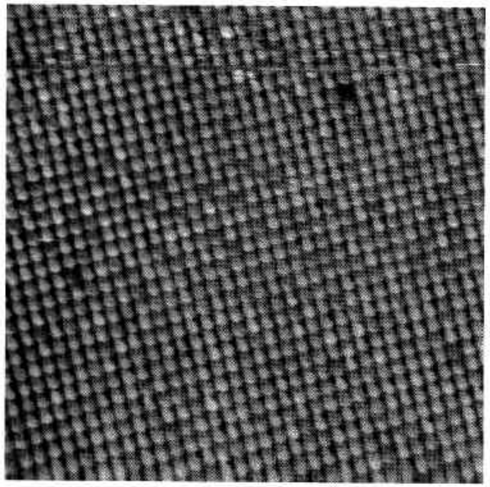

FIG. 49. Unreconstructed Au(100) on Au_3Pd single crystal after 800 K anneal; 90 Å, −0.3 V, 1.7 nA [46].

TABLE III. Summary of the Structures Observed by STM on Pt_3Sn Surfaces After Annealing at Moderate and High Temperature

	600–800 K	1000–1100 K
(111)	$(\sqrt{3} \times \sqrt{3})$ R30° (Pt_2Sn), mesoscopic subsurface dislocation network	p(2 × 2), adatom islands
(100)	multiple row structure, pyramids bordered by {102} and {104} facets	c(2 × 2), double steps, single atomic ad rows
(110)	hill and-valley-like structure with {102} facets	(2 × 1), double steps, holes at Sn positions

In alloys of the other category, the preferentially sputtered component is segregating towards the surface. Here Pt_3Sn serves as an example, in which Sn is segregating and preferentially sputtered ($m_{Sn} < m_{Pt}$ and $T_{Sn} < T_{Pt}$). The Pt_3Sn exhibits a strict chemical order of the $L1_2$ type, that is, fcc structure with Pt at the corner sites and Sn at the face sites of the unit cell. The depletion in Sn in the surface region leads to a smaller lattice constant ($a_{Pt} < a_{Pt_3Sn}$). All three low-indexed surfaces of Pt_3Sn respond to this depletion by formation of metastable phases with characteristic stress compensation features (Table III). A mesoscopic dislocation network, pyramids, or ripples are formed on the different surface planes (111) [91], (100) [89], and (110) [92]. All these structures could not be identified in earlier LEED analyses [90, 170, 171]. The pyramidal phase of $Pt_3Sn(100)$ is shown in Figure 50. The facets of the pyramids are of {102} and {104} orientation. Despite the depletion in Sn in the surface region, in the outermost surface layer the Sn concentration is enhanced. For instance, the outermost layer of $Pt_3Sn(111)$ has the composition and structure of Pt_2Sn. This Sn excess can be

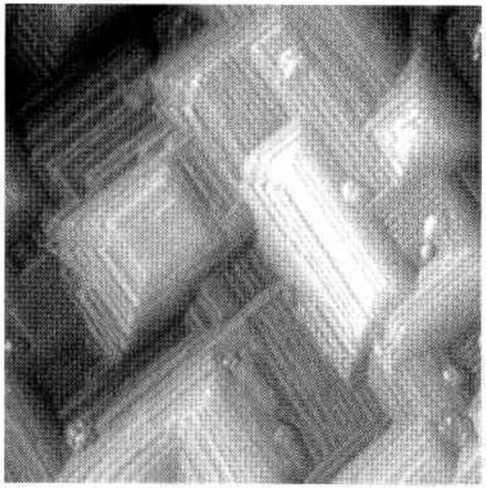

FIG. 50. Pyramidal phase of the $Pt_3Sn(100)$ surface after 620 K anneal; 700 Å, 0.6 V, 1 nA [89].

attributed to the higher surface energy of Sn-rich surfaces. The surface energies of pure Sn and Pt are 0.61–0.62 J/m^2 and 2.3–2.8 J/m^2, respectively [172].

The equilibrium phase of the three Pt_3Sn surfaces develops after annealing to temperatures as high as 1000 K. The STM measurements, and also LEED and LEIS [90, 170], revealed that only the mixed PtSn planes of $Pt_3Sn(100)$ and (110) are observed. In the bulk these planes are stacked in layers with alternating composition of PtSn and pure Pt. Thus, bulk-truncated PtSn terraces can only be separated by doubles or multiples of double steps. This is, in fact, observed in STM images. No steps of heights corresponding to odd numbers of layers have been found [89, 92]. In contrast, fcc(111) planes have homogeneous composition and stacking. Thus, monoatomic step heights are compatible with the bulk-truncated $Pt_3Sn(111)$ surface structure in this case. This is in line with the observations that is, STM topographies that show exclusively monoatomic steps.

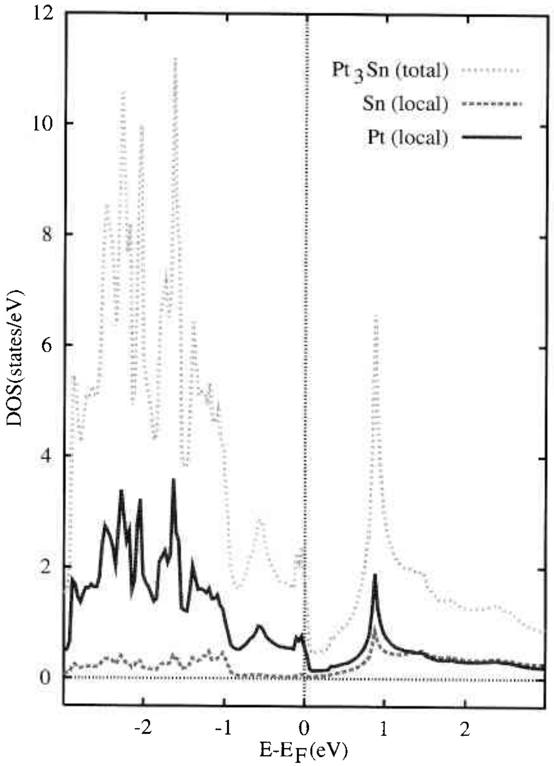

FIG. 51. Total (per unit cell) and local (per space-filling atomic spheres of equal size at both Pt and Sn sites) densities of states of Pt_3Sn, calculated by the tigh-binding linear muffin-tin orbitals method. At positive (sample-) bias voltages the unoccupied states above E_F are imaged in the STM. Reprinted with permission from [89], © 1999, The American Physical Society.

All surfaces have in common that the Sn between the Pt is not imaged as a bump in the STM topography but as a depression. The origin of this strong chemical contrast is the large difference in the electronic structure. Band structure calculations reveal that in the region near the Fermi level the density of states at the Sn atoms is clearly lower than that at the Pt atoms (Fig. 51). To illustrate this effect, the STM topography of the $Pt_3Sn(110)$ surface is shown in Figure 52. The bumps are the Pt atoms and the Sn atoms are the weak depressions in between. Note that due to the "invisibility" of the Sn the apparently more densely packed rows run along ⟨100⟩. Holes in the form of monolayer deep depressions are observed only at the Sn positions. As the sublimation of Sn is probably stronger than of Pt and the stability of single vacancies is usually low, an adatom gas depleted in Sn is the most plausible explanation for the holes in Figure 52 [92]. Discrimination between two atomic species by STM is not obtained with any system and tip. Initially, chemical contrast was obtained on PtNi alloys [173].

5.2.4 Ultrathin Films. The demand for artificial materials or so-called designer solids is increasing. Many applications such as solid state lasers and new generations of transistors require ever finer structuring of materials. It is very common for the properties of devices based on heterostructures to depend on the quality of the interfaces. The structures can be grown by chemical vapor deposition (CVD) or molecular beam epitaxy (MBE). Transmission electron microscopy

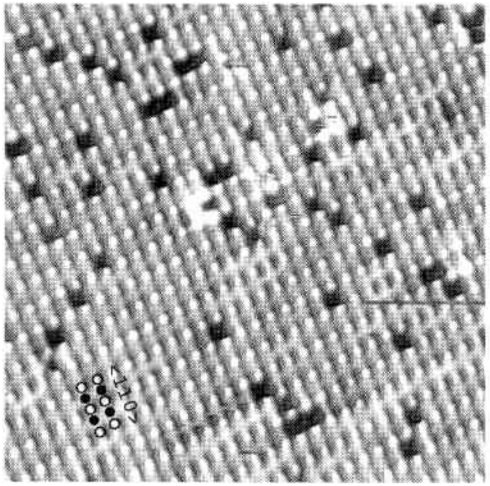

FIG. 52. An STM image of the $Pt_3Sn(110)$ surface; 120 Å, 0.5 V, 0.8 nA. The Pt atoms are visible as protrusions (open circles), the Sn atoms are invisible (filled circles).

(TEM) and RHEED (see Section 3.2) are the standard methods used to check the crystallinity of the layers and interfaces. However, the origins for imperfect crystallinity of thicker films are not directly inferrable from such analyses. Here, understanding the evolution at the onset of growth is the goal. Besides preparation of nanostructures with novel physical properties in general, this is one of the major motivations for studying the topography and structure of incomplete layers by STM. An overview of the nucleation and aggregation of thin metal layers is given in Reference [174].

With regard to magnetoelectronics, structures of nonferromagnetic combined with (anti)ferromagnetic materials are of special interest (see also Section 4.6). As an example, we show in Figure 53 an STM image of 0.12 ML Cr on Cu(111) [175] grown by thermal evaporation. The structure is similar to Co/Cu(111) [176, 177] and Fe/Cu(111) [178]. Although Cr and Cu are not miscible in bulk, etching of the substrate occurs. Vacancy islands are observed in the vicinity of steps after initial growth. Such rearrangement contributes to interfacial roughness. It is driven by a decrease in total energy because material of lower surface energy is going to cover material of higher surface energy (Cr, Co, Fe). This process can be extenuated when the initial growth is performed at low sample temperature [179].

In Figure 53 the steps are decorated by approximately 50-Å wide Cr bands of bilayer height, measured from the upper terrace. Similar step decoration in the form of interrupted island bands was found with Co/Cu(111) [176], Fe/Cu(111) [178], and Ni/Ag(111) [180]. The islands that have agglomerated in the middle of the terraces are also of bilayer height. Studying thicker Co films by STM and LEED revealed that one fraction of the islands occupies fcc positions and another fraction hcp positions on the Cu(111) substrate [177]. This twinning in nucleation causes problems in thick films, when the different types of islands cannot connect and canyon-like defects remain.

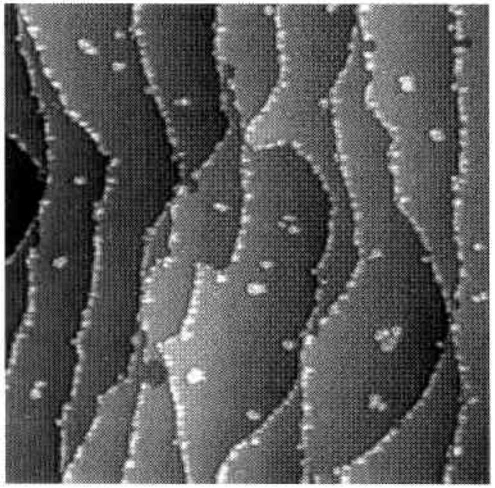

FIG. 53. 0.12 monolayers Cr on Cu(111). The height of the Cr bands at the steps is 4 Å, measured from the upper terrace. The height of the islands is 4 Å. The small indentations at the steps are caused by missing substrate material due to intermixing between Cr and Cu; 3000 Å, 2.7 V, 0.07 nA.

Another challenge is the production of 1D structures that might exhibit totally different magnetic properties [181]. Such lateral systems can be obtained by step decoration on vicinal surfaces.

Here we give an example using substrates with terraces of nanoscopic width. This will suppress the formation of the typical form of decoration bands of incompletely connected islands as observed on the low indexed (111) surfaces. There are striking differences in the morphology of vicinal surfaces with {100} and {111} step minifacets. The most remarkable effect of the Co is that on the surfaces with the {100} steps the step array is rearranged into a configuration where double steps prevail (Fig. 54). These rearrangements afford considerable mass transport in the substrate surface. The double steps do not exhibit frizziness. Prior to deposition only single steps in a regular step array similar to those shown in Figure 47 were observed. In principle, double steps can also result after exposure to oxygen [182]. On the basis of AES (see Section 4.3) and CO adsorption experiments we attribute the double steps shown in Figure 54 to incorporated Co. The Co agglomerates appear immobile, probably as a consequence of the stronger binding compared to Cu. Thus, kink diffusion becomes slow compared to the usual STM sampling rates of some kHz when Co is involved. Note also that at the double steps only immobile, that is, "frozen" kinks (labeled f in Fig. 54) are observed to display a width of multiples of $a_\perp$. The topography at the merging points (labeled Y in Fig. 54) reminds one of a zipper and suggests that the incorporation of Co in {100} step minifacets also works like a zipper [183]. Most likely these double steps at the {100} minifacets represent a 1D alloy. This interpretation is according to the Co structures observed on the large counterparts, the low-indexed Cu(100) surface: According to an STM and a density-functional theory study Co occupies substitutional sites in the flat Cu(100) substrate [184].

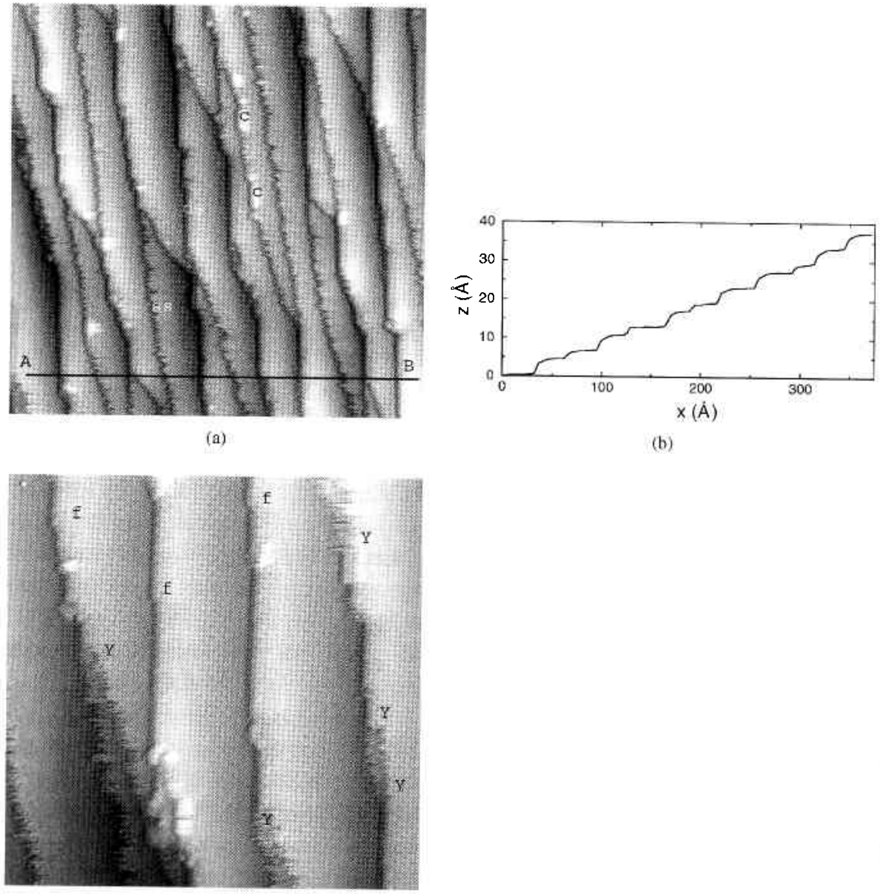

(a) (b) (c)

FIG. 54. Cu(111) surface with 5° miscut, {100} steps and low Co coverage. (a) 385 Å, −0.3 V, 0.7 nA, "ds" marks a double step, "ss" marks a single step and "c" marks very rare positions where single steps are unfrizzy, possibly due to contaminants; (b) line scan $z(x)$ of image (a); (c) 185 Å, −0.3 V, 0.7 nA. The "beady" step edges contain Co and have double height. The labels Y and f mark transition points from double to single steps and frozen kinks, respectively.

5.2.5 Adsorbate Layers. The background of applications behind the study of adsorbate layers is heterogeneous catalysis where surfaces are used to accelerate chemical reactions. Examples for reactions to be accelerated are the detoxication processes in exhaust gases, for example, $O_2 + 2CO \rightarrow 2CO_2$, and the industrial production of technical gases. The aim is to understand catalytic surface reactions on an atomic level, that is, the ability to improve catalysts systematically. One element in such analyses is the study of adsorbate layers by STM [185–187].

Because sticking coefficients are material dependent, adsorption allows marking and titration of elements. As an example, Figure 55 shows the topography of $Pt_3Sn(110)$ after CO adsorption. The CO is found on top of the Pt bumps but never between them, at the Sn positions [188]. Thus, in addition to catalytic applications, adsorption experiments provides a method to discriminate between elemental species.

In many catalysts sulfur acts as a poison, which necessarily motivates study of S layers on catalytically interesting surfaces. To produce S layers on surfaces,

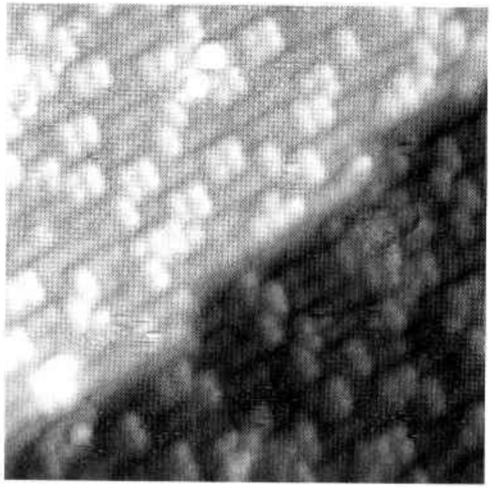

FIG. 55. The $Pt_3Sn(110)$ after exposure to 60 L CO; 120 Å, 0.4 V, 0.8 nA. The CO is found on top of the Pt bumps, never in between at the Sn positions. The carbon side binds to the Pt substrate atoms and the molecules are arranged in dimers and tetramers.

H_2S adsorption can be used because upon dissociation the S stays at the surface whereas the H is believed to desorb or be incorporated in the subsurface. Adsorbates can appear as protrusions or depressions, or they can be invisible in STM topographies and thus theoretical predictions [189] must be employed for interpretation.

A somewhat uncommon approach to production of adsorbate layers is to exploit the impurity atoms in the crystal that segregate to the surface during annealing to higher temperatures ($T_{\text{anneal}} \approx 0.5 \cdot T_M$). For instance, most Pd crystals contain S impurities. Annealing to >800 K results in 0.15-0.34 monolayers S at the surface. The adlayer is partly disordered and the steps are decorated with (2 × 2) bands [190] (Fig. 56a). In the (2 × 2) structures the sulfur atoms prefer acute angles (30°). This is reflected in the shape of the step bands and the triangles. The origin of acute angles in the structures is the even valency of the sulfur.

Interestingly, neither the decoration bands nor the triangles are reproduced when the sulfur films were produced by 2-3 Langmuir exposure to H_2S gas (Fig. 56b). Instead the (2 × 2) structures form patches with bands. A structure developing only with adsorption is the ($\sqrt{3} \times \sqrt{3}$) R30°. The other structures as the ($\sqrt{7} \times \sqrt{7}$) R19.1° and the disordered structures are also obtained by adsorption. When annealing to higher temperatures (>400 K) the ($\sqrt{7} \times \sqrt{7}$) R19.1° displaces the other structures to a large extent [191]. Thus, only the ($\sqrt{7} \times \sqrt{7}$) R19.1° structure is an equilibrated state.

5.2.6 Organic Films. The fields of applications behind layers of organic molecules are biolelectronical interfaces, electronic devices like transistors, light emitting diodes (LED), lasers, and electronic wiring. The advantage of organic light emitting diodes (OLEDs) [192, 193] compared to conventional LEDs on a semiconductor basis are the flexibility of the material and the relatively easy tuneability of the gap, that is, the color. The length of suitable molecules, like multinary phenyls, exceeds 20 Å such that the low conductivity through such a layer often makes STM difficult and such films are usually studied by AFM (Part IV) [194, 195].

5.2.7 Nanostructures. In 1959 Feynman brought up the idea of miniaturing machines down to the atomic level [196]. Surfaces are an especially nice playground for the realization of controlled fabrication of ordered structures with nanometer dimensions. The prerequisite step involves overcoming the limits of conventional optical lithography (≈200 nm). Today it has become possible to fabricate many of such nanostructures but they are not yet part of everyday products. Since STM and AFM are extensively used to image nanostructures on surfaces we illustrate in the following a few aspects of this field.

Without any precautions, islands typically agglomerate at rather random positions on the surfaces, governed by nucleation and agglomeration processes. Ordered nanostructures can be obtained when the film is grown on mesoscopic network structures arising from reconstructions or stress compensation. An early example is the growth of Ni islands at the "elbows" of the Au(111) ($\sqrt{3} \times 22$) reconstruction [197] shown in Figure 57. An example for ordered islands using a 2D defect pattern is given in Reference [198]. A strain relief network is formed after 800 K annealing for a monolayer Ag on Pt(111). A second Ag layer nucle-

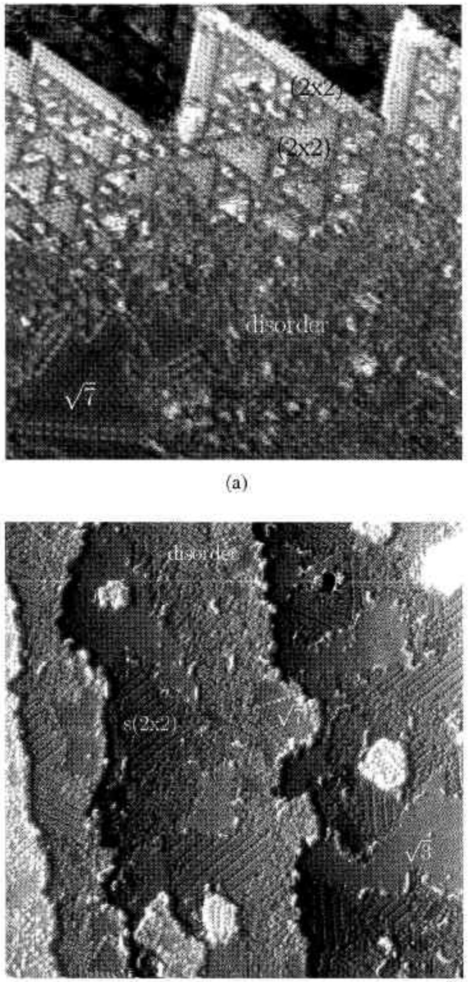

(a)

(b)

FIG. 56. Sulfur layers after segregation (a) and H_2S adsorption (b) on Pd(111). The parameters are 400 Å, −0.07 V, 1.0 nA and 640 Å, −0.05 V, 2.0 nA. Visible are (2×2)triangles, (2×2)step decoration bands, disordered areas, and ($\sqrt{7} \times \sqrt{7}$) R19.1°. Areas with decorated domain boundaries (a) and disordered, $\sqrt{3} \times \sqrt{3}$R 30°, ($\sqrt{7} \times \sqrt{7}$) R19.1°; and striped (2 × 2) areas (b).

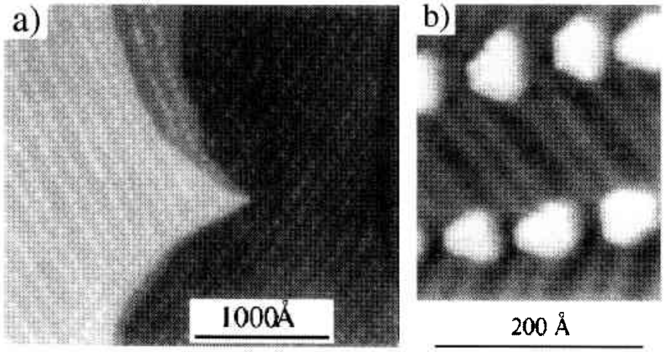

FIG. 57. The 0.1 monolayers Ni on Au(111). The islands grow at the elbow sites of the ($\sqrt{3} \times 22$) reconstruction of Au(111) [197]. Reprinted with permission from D. D. Chambliss et al., *Phys. Rev. Lett.* 66, 1721 (1991), © 1991, The American Physical Society.

ates predominantly inside the fcc meshes and a regular pattern of Ag islands, that is, of zero-dimensional structures, results (Fig. 58).

The 1D counterparts are epitaxial bands that grow at steps on surfaces. These "wires" can be more or less smooth. For instance Cu grows on stepped W(110) and Mo(110) in bands at the lower sides of the steps. On W(110) the new Cu step edge of these bands appears rough compared to the original step edge (1D Stranski-Krastanov) whereas on stepped Mo(110) the Cu bands display smooth edges (1D layer-by-layer) [199]. Contrast between these different metals was managed in STM images by resonant tunneling via surface states and image states. This is a nice example of how identification of the elements by STM can be achieved via knowledge about the electronic structure of the materials. Equally fascinating are purely electronic low dimensional structures. Clean self-ordering steps as described in Section 5.2.2 represent a set of 1D nanostructures and can 1D lead to confinement and hybridization effects [200].

An elegant way to produce ordered nanostructures is atom lithography through a light field of standing light waves in front of the substrate. The resulting structures can be arranged according to any possible pattern of the light field, that is, rows, dots, zig-zag, honeycombs, pearl necklets [201, 202].

One of the special features of nanostructures is that the dimensions of such structures are of the order of the wavelengths of electrons in metals such that quantum effects dominate. The first and most impressive realization is the quantum corrals on Cu(111) arranged by Xe atoms at low temperature [203]. The Xe atoms could be attached and deattached to the STM tip in a controlled manner by means of voltage pulses. The electron waves of the Cu(111) surface state are partly reflected at the inside of the Xe boundary and a standing wave pattern forms

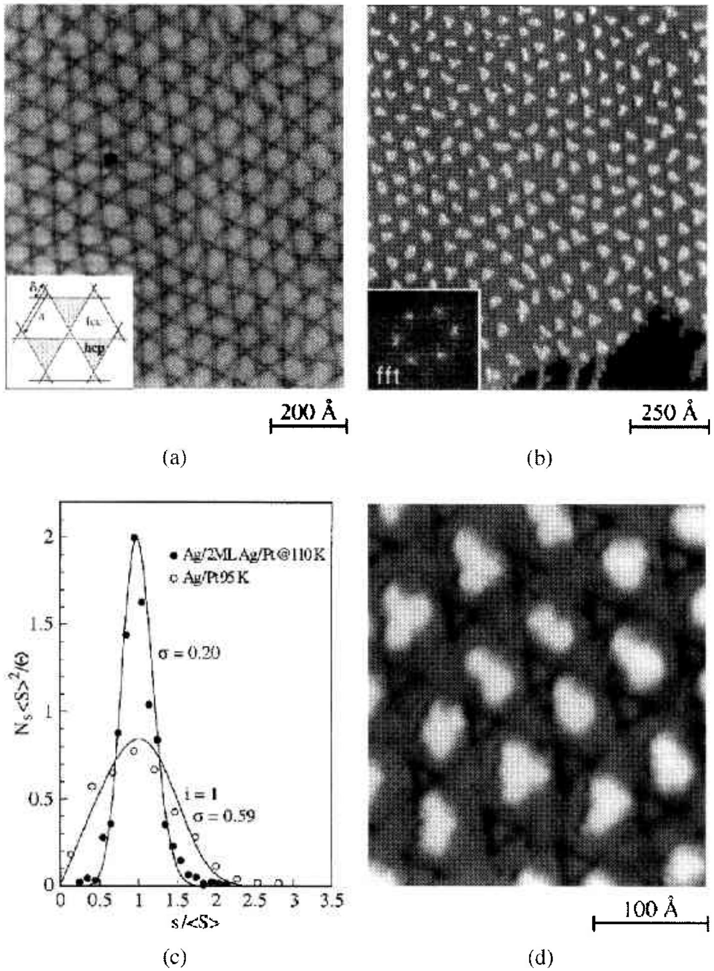

FIG. 58. Confinement nucleation of adatom islands on a dislocation network. (a) Ordered (25 × 25) dislocation network formed by the second Ag monolayer on Pt(111) on deposition at 400 K and subsequent annealing to 800 K. The inset shows a model of this trigonal strain relief pattern. (b) A superlattice of islands is formed on Ag deposition onto this network at 110 K (coverage = 0.10 monolayers). The inset shows the Fourier transform of the STM image. (c) Island size distributions for random and ordered nucleation. The curve for ordered nucleation is a binominal fit. The curve labeled $i = 1$ shows the size distribution from scaling theory for random nucleation on an isotropic substrate. Size distributions were normalized according to scaling theory (s is the island size in atoms, $\langle S\rangle$ its mean value, and N_S the density of islands with size s per substrate atom). (d) Zoom into image (b) [198]. Reprinted with permission from H. Brune et al., *Nature* 344, 451 (1998), © 1998, Macmillan Magazines Ltd.

that can be imaged by STM. These were the first real space images of electronic states. The latest attainment by such structures is the mirage Co atom imaged by STM inside a corral of such type [204]. If one real Co atom is placed at a focus point of an elliptical corral, due to the Kondo resonance, some of its properties appear at the other focus, where no atom actually exist.

Standing electron wave patterns of surface states also can be observed in defects. This was realized with adatom islands on Ag(111) at low temperature [205]. Vacancy islands did not show electron confinement probably because of absorption losses via bulk transitions.

5.3 Scanning Tunneling Spectroscopy

Scanning tunneling spectroscopy (STS) allows local electronic properties to be determined. The tunnel current I (Eq. (47)) depends on two variables, the voltage U and the tip-sample-separation ($\propto z$). Hence, there are three modi of local spectroscopy $I(U)$, $I(z)$, and $U(z)$, with the third parameter being kept constant. The $U(z)$ spectroscopy is rarely used because I is a dependent variable and it is difficult to keep it constant when the two other parameters vary.

5.3.1 Local Work Function. $I(z)$ and $U(z)$ spectroscopy allows one to determine the mean barrier height $\bar{\Phi}$ that is related to the local work function. The acquisition of such spectra is made at each scan point. Once, before taking the spectroscopic curve with the regulation loop deactivated, z is adjusted according to the setpoint current. With Eq. (47) the average barrier height is

$$\bar{\Phi} = \frac{\hbar^2}{8m}\left(\frac{\Delta \ln(I/I_0)}{\Delta z}\right)^2 = \frac{\hbar^2}{8m}\left(\frac{\Delta \ln(U/U_0)}{\Delta z}\right)^2 \qquad (50)$$

$$\text{with} \quad \bar{\Phi} = \frac{\Phi_{\text{probe}} + \Phi_{\text{sample}}}{2}$$

Due to the image charge the barrier height is lowered by a few eV, compared with work functions of the free surfaces.

For free surfaces the local work function is usually lowered at steps on metals due to Smoluchowski smoothing [160]. The spatial width of such line dipoles can be determined only from STS work function maps. With steps on Au and Cu surfaces a reduction of the work function in an approximately 8 Å wide zone was observed [206]. Figure 59 shows an STM image and a work function map of 0.8 monolayers Au on Cu(111). Nonlocal methods, for example, traditional photoelectron spectroscopy, simply yield a lowered average work function for stepped surfaces.

5.3.2 Local Density of States. Acquisition of a characteristic $I(U)$ curve at constant z piezolength, that is, with the feedback loop switched off, allows us to obtain qualitative information on the local density of states (LDOS) of a surface. The quantitative context of LDOS and characteristic $I(U)$ curves is not completely clear. There are plenty of suggestions as to how to calculate a curve from $I(U)$ in order to obtain maximal similarity with the LDOS. With metals and low gap voltages (<1 V) the local differential conductances are calculated to this purpose [207, and references therein], that is, $\rho_{\text{sample}}(E) \propto dI(U)/dU$.

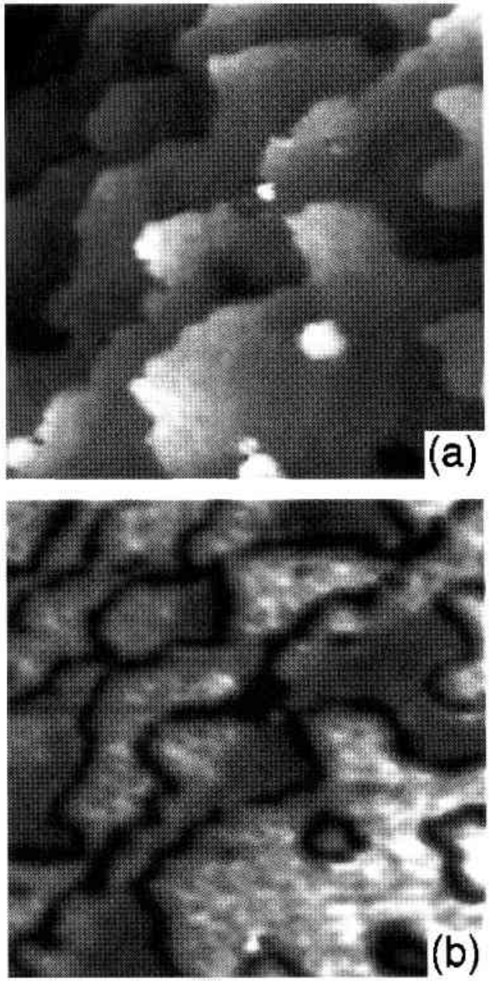

FIG. 59. (a) The STM image 580 Å, −2.0 V, 0.1 nA, obtained from the Au/Cu(111) surface with 0.8 ML of Au. (b) Local work-function image obtained simultaneously with (a). A higher brightness represents a higher local work function [206]. Reprinted with permission from J. F. Jia et al., *Phys. Rev.* B58, 1193 (1998), © 1998, The American Physical Society.

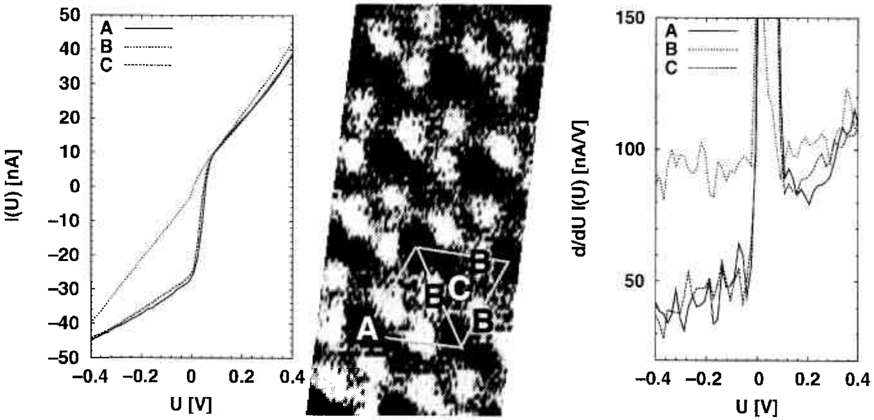

FIG. 60. Atomically resolved STS measurements of the $(\sqrt{7} \times \sqrt{7})$ R19.1 ° structure. A,B,C positions refer to S_{fcc}, Pd and S_{hcp} atoms, respectively. $I(U)$ curves (left). Drift corrected I image at $U_0 = -0.1$ V (middle). $(d/dU)I(U)$ curves (right) [209]. Reprinted with permission from S. Speller et al., *Phys. Rev. B* 61, 7297 (2000), © 2000, The American Physical Society.

This is the simplest, qualitative extension of Eq. (49) when ignoring the variation of the transmission T with energy. With semiconductors and higher gap voltages the normalized differential conductance $\rho_{\text{sample}}(E) \propto (dI/dU)/(I/U)$ is used [208]. Such $\rho_{\text{sample}}(E)$ curves reproduce pronounced features of the real density of states.

We illustrate the spatially varying LDOS by means of the $(\sqrt{7} \times \sqrt{7})$ R19.1° layer of sulfur on Pd(111) [209]. Figure 60 shows characteristic curves that are taken at different positions in the S layer. Within the empty states (<0 V) a lower current and $dI(U)/dU$ is found when measured on S atoms. This reduced electron density can be understood by means of the LDOS calculated by the full potential linear augmented plane wave (FLAPW) method [209].

5.3.3 Vibration Spectroscopy.

Vibrations of molecules on surfaces can be excited by the tunneling electrons when the corresponding eigenenergies ($h\nu$) are surpassed by the energy corresponding to the gap voltage (eU). The conductance is then raised by this small fraction of inelastic tunnel processes. Such information is hence available by inelastic electron tunneling spectroscopy (IETS) from $I(U)$ curves. Calculating $d^2I(U)/dU^2$ yields small peaks at the energies of the vibration frequencies of the molecules [210]. As with other STS methods, the traditional (nonlocal) IETS spectroscopy had already been developed much earlier [211].

PART IV. ATOMIC FORCE MICROSCOPY

The AFM was developed a few years after STM [212]. A special feature is that no tunnel current is needed and thus insulators, for example, salts, glasses, layers of organic molecules, or crystals of biological molecules and complete biological objects can be studied. For AFM, the probe is mounted on a lever that bends under the force of the sample surface (Fig. 61). For technical reasons, in most AFMs the sample is attached to the fine piezoelements, and hence the sample is scanned against the tip, which is the opposite of what is done with traditional STM. The bending of the lever can be measured by means of a piggyback STM, an interferometer, or a light pointer. Nowadays, the light pointer principle is commonly used: The beam from a light emitting diode is reflected at the end of the cantilever onto a 2D position sensitive detector (PSD). The deflection is approximately proportional to the applied force. This technique allows discrimination between the normal force F_z and lateral forces F_x and F_y. Meanwhile, combined AFM/STM heads and AFMs operating in gases, vacuum, or liquid cells are commercially

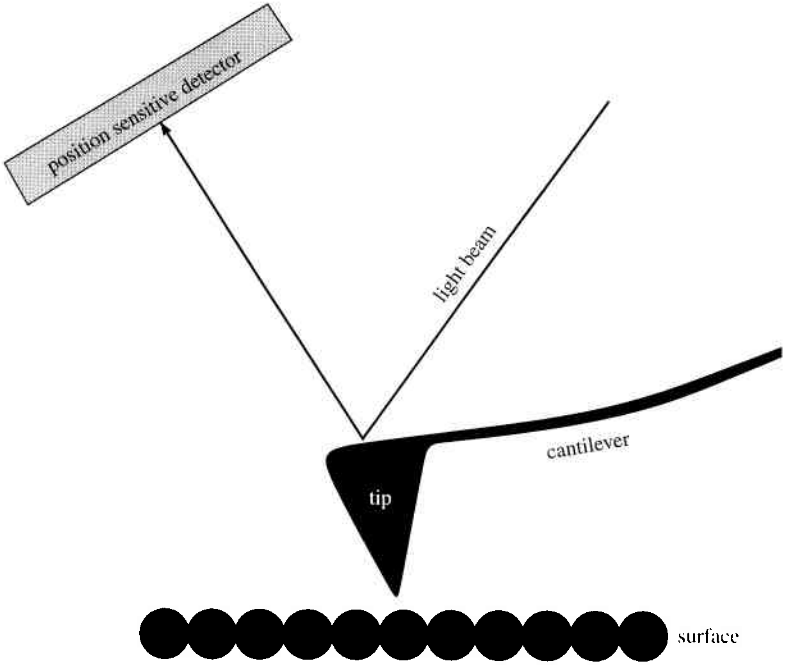

FIG. 61. Illustration of the AFM method (not to scale)

available. A millipedelike ultrahigh density data storage concept has been developed on the basis of AFM [213].

A variety of forces act between tip and sample atoms (see Table IV). The potential is Lennard-Jones-like

$$\Phi(d) = -\frac{A}{d^6} + \frac{B}{d^{12}}$$

a superposition of a short-range repulsive and a long-range van-der-Waals attractive part (Fig. 62a). This potential does not comprise magnetic, electrostatic, and hydrofluid contributions. The negative gradient of such a potential gives the force that governs the deflection of the lever (Fig. 62b). The derivative of the force-distance curve gives the force constant curve.

TABLE IV. Overview of Important Interactions Occuring Between Tip and Sample Atoms in the Atomic Force Microscope

Interaction type	Nature	Range
Pauli exclusion	Short range, repulsive	≈ 0.1 nm
Coulomb repulsion (cores)	Short range, repulsive	≈ 0.1 nm
Chemical bond	Short range, attractive	≈ 0.1 nm
Van der Waals	Long range, attractive	Up to 100 nm
Electrostatic	Long range, attr. or rep.	≈ Several 100 nm
Magnetic	Long range, attr. or rep.	≈ Several 100 nm
Capillary forces	Attractive	Up to 10 nm
Hydrodynamic	Very long range, damping	≈ 10 μm

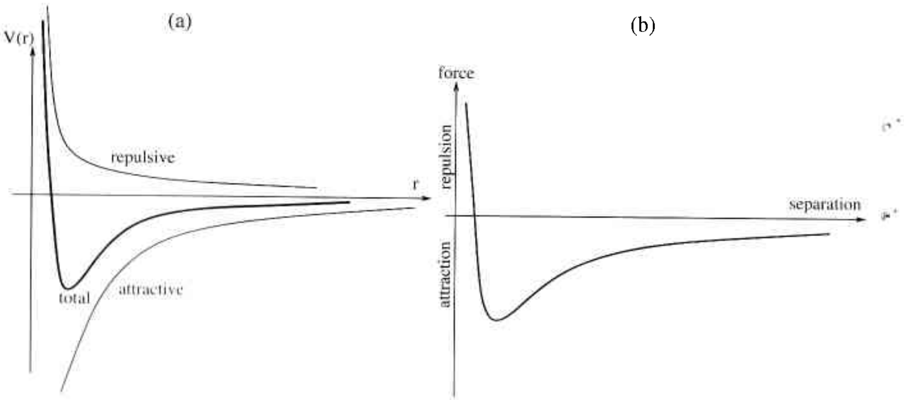

FIG. 62. Variation of the potential between tip and sample with distance (a) and the variation of the force between tip and sample with distance (b).

5.3.4 Force-Distance Curves. Measuring force-distance curves (Fig. 63) of samples gives a completely different image because since the distance (abscissae) refers to the relative z piezoposition and not directly to the position of the cantilever tip. There are two discontinuities in the force-distance loop that reflect points of instability, points (1) and (3) in Figure 63. During approach, no force is initially active. At point (1) the surface's (attractive) force gradient surpasses the lever's spring constant and the lever jumps towards the surface, into contact, to the repulsive force regime. As this jump takes place only at the tip and not at the z piezo a sudden change in force without any z change is noticed in the force-distance curve. Therefore, the shapes of the force curve inferred from the potential and the measured one differ (Figs. 62b and 63). In contact, the lever is pushed by the sample (points (2) to (3)). Upon further approach of the sample the normal force increases linearly according to the spring constant of the lever. When the sample is being retracted, the slope of the force curve is slightly different. The main reason is piezo creep. Close to point (3) the force is maximally attractive and the spring constant is surpassed a second time. The lever jumps back and is then again in an interaction free point (4), far from the surface.

The area between approach and retract curves (hysteresis) reflects the energy loss of the cantilever, for example due to deformation of the surface. The shape of force-distance curves changes when repulsive forces dominate (no jump-to and jump-off) or when measuring in liquids.

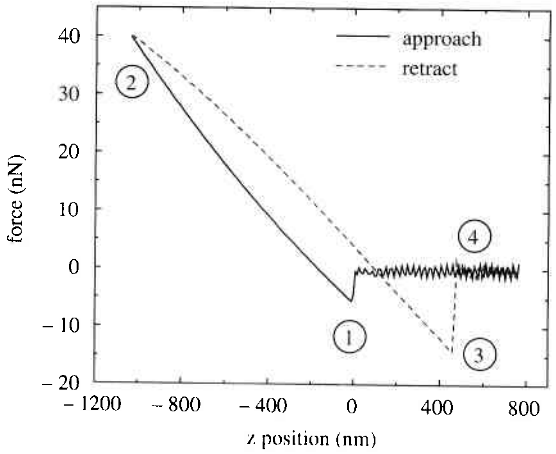

FIG. 63. Force distance curve on Si(111) covered with a self-assembled octadecyl trichlorosilane layer.

The force constants of levers can be calculated from the geometrical dimensions and Young's module. Therefore, force-distance curves allow calibration of the AFM forces with respect to the voltages at the PSD.

The interaction force versus the tip-sample distance can be calculated partly from force-distance curve. The distance-values are transformed such that the contact line $F(z) = -k \cdot z + F_0$ becomes the ordinate of the interaction force curve.

5.3.5 Contact Mode. In contact mode a constant normal force, typically in the nN-range, is maintained via a regulation loop. Similar to STM this is done by adjusting the z-piezo accordingly. The force must be calibrated for every new cantilever via a force distance curve (see Section 5.3.4). With hard materials the measured surfaces of constant force represent the topography. However, contact measurements are destructive to a certain extent. Problems arise especially with soft materials, because material is moved or destroyed by the applied forces during the scan. This is already true for metals such as Au.

Alternatively, the contact mode can be operated in the error signal mode by slowing down the regulation speed and collecting the normal force signal directly. This mode is the analog to the CHM in STM. The images show higher contrast, but are not quantitatively related to the topography.

5.3.6 Lateral Forces and Friction Maps. Frictional forces show up as a systematic asymmetry between the structures of two images taken at backward and forward scan. This can be observed in the AFM (and STM) topography, for example, on HOPG.

The variations in friction between the tip and sample causes a stick and slip movement of the lever's tip. If the fast scan direction (x) is perpendicular to the lever axis this results in lever torsion. Deflection of the light beam by a twisted lever on the position sensitive detector is perpendicular to the usual deviation stemming from normal (z) forces. Thereby, discrimination of F_x and F_z is possible. Lateral force microscopy (LFM) measures the forces parallel to the surface plane. The feedback loop must be slowed down, as always when a force channel is measured.

Changes of F_y and F_z deflect the light beam in the same direction. The cantilever is then buckled, which must distort the topography signal. In certain cases, one may assume that the frictional force dominates the normal force and a F_y-map can be aquired. A clean topography signal is not possible in this scan geometry. On the other hand, if the surface is not atomically flat, the cantilever will additionally be twisted when the slope of the surface changes. To separate such topographical from frictional origins LFM and AFM images should be taken simultaneously.

However, terraces that exhibit the same appearance in topography can show different lateral force signals. This is attributed to a sort of material contrast or different nanoscopic roughness [214].

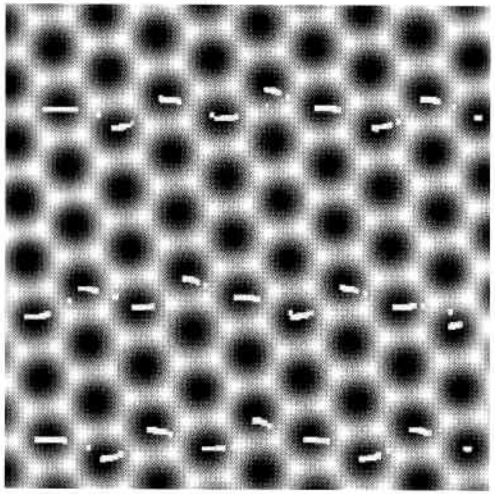

FIG. 64. Gray scale plot of the interaction potential on HOPG (image size 20 Å) and three typical calculated paths of the tip in this potential plotted by dots separated by equal time intervals ($\Delta t = 0.1$ ms, $v = 40$ nm/s) [215]. Reprinted with permission from H. Hölscher et al., *Phys. Rev.* B57, 2477 (1998), © 1998, The American Physical Society.

A nice illustration for the stick-and-slip process is the trajectory of the cantilever on HOPG. For many years it remained puzzling as to why only one type of carbon atom was visible by scanning methods. In the case of AFM this seems to be solved by comparing LFM maps with simulations [215]. Figure 64 shows the interaction potential and three typical calculated paths of the tip in this potential plotted by dots separated by equal time intervals. The bright positions show the atomic honeycomb surface lattice. In LFM, AFM and STM images a simple hexagonal structure similar to the black position is observed. Although the scan speed is constant, the tip moves discontinuously over the surface and stays most of the time in the minima (dark areas), that is, between the atoms. This stick-and-slip movement causes the force maps to represent "hollow-site resolution" instead of "atomic resolution."

5.3.7 Noncontact Mode. In the noncontact mode the influence of the force gradient between probe and surface on a vibrating cantilever is utilized to measure the topography. The tip-sample separation is large, typically between 1 and 100 nm. In contrast to the contact mode, the noncontact mode is less destructive. The cantilever oscillates, driven by a quartz. In air the lever vibration is damped more strongly and it is very difficult to avoid a jump-to-contact through a meniscus of the thin water film that is always present in air. Therefore, noncontact measurements generally require vacuum conditions. Even at the reversal points of the vibration the tip should not touch the surface, that is, the amplitude of the oscillation must be kept small. An intermediate mode when that is not fullfilled, that is, with intermittent contact, is called the tapping mode. This is often used in air or gases when imaging poorly immobilized or soft samples. Both methods are dynamic modi.

The force gradient $F' = dF/dr$, from the interaction between surface and tip (see Fig. 62a,b), is measured via the shift in resonance frequency. This shift serves as the feedback signal. The harmonic approximation is only valid with fairly small amplitudes because the potential in front of the surface is highly asymmetric. The force gradient is varying with distance from the sample, and alters the effective spring constant, $k_{\mathrm{eff}} = k + \Delta k$ with k being the spring constant of the free cantilever. At a certain tip-sample separation r_1 the total force gradient becomes $F' = k_{\mathrm{eff}} \approx k - dF/dr(r_1)$. Accordingly, the resonance frequency shifts to $\omega_0^* = \sqrt{k_{\mathrm{eff}}/m_{\mathrm{eff}}}$ with m_{eff} being the effective mass of the cantilever.

The quality factor of an oscillation is defined by $Q = \sqrt{\gamma m}/k$ with γ being the damping coefficient. If the damping is small the Q factor equals the quotient of the eigenfrequency of the free cantilever and the width of the resonance maximum at the so-called half power point (HPP) (where the amplitude has decayed to $A_{\mathrm{HPP}} = A_{\max}/\sqrt{2}$): $Q = \omega_0^{\mathrm{free}}/\Delta\omega_{\mathrm{HPP}}$. In air the Q factors are typically between 100 and 1000. In UHV they are approximately 100 times larger.

5.3.8 Principles of Force Gradient Detection.

5.3.8.1 Slope Detection. Slope detection is often used for AFMs operated in air. The cantilever is then driven at its free eigenfrequency. After the approach the amplitude decreases by ΔA due to its being out of tune. The reduced amplitude is detected and used as the feedback signal (see Fig. 65). The z piezoadjustment, necessary to keep the amplitude at the setpoint value (e.g., 80% of A_0), gives the topography. As the lever is not operated in resonance, the phase lag of the oscillation against the excitation shifts away from $\pi/2$, the magnitude of this shift dependent upon local damping. This shift $\Delta\Phi$ is often coimaged as an additional information channel. Although is not completely clear what physical information this extra channel carries, it is very rich in contrast and is not dominated by the relatively large topographic variations. It might be interpretable as material or chemical contrast.

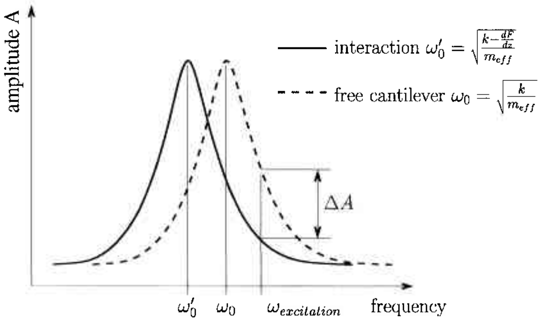

FIG. 65. Illustration of the slope detection principle by means of the resonance curve of the lever. In the vicinity of a sample the resonance frequency shifts and leads to a reduced amplitude at the excitation frequency.

5.3.8.2 Frequency Modulation Detection. With a sharp resonance curve, as in UHV, the amplitude drops too quickly to zero under the presence of a force field. Regulation of ΔA is therefore not possible. Instead, in the frequency modulation (FM) mode the cantilever is vibrating freely with its respective resonance frequency ω^* including the local force gradient. Such an oscillation must be self-excited, that is, part of the oscillation signal itself is fed back, correctly phase-shifted, to a modulation piezo behind the cantilever. In this way maximal resonance is maintained and the amplitude is regulated to a constant value by an extra feedback circuit. However, the actual feedback signal is the frequency shift. Hence surfaces of constant force gradient are measured during the scan. The advantage is that the frequency shift is more directly related to the interaction force than the amplitude in slope detection is.

5.3.9 Probes.

Due to its hardness and stiffness Si_3N_4 probes have been widely used for contact force microscopy. Microfabricated force sensors with an integrated tip are commercially available. They are etched out of Si wafers and the outermost layer can either be covered by a Si_3N_4 film or oxidized. For combined STM/AFM UHV applications this film can be sputtered off to make the cantilever conductive again. Depending on the dimensions, the eigenfrequencies vary between 10 (contact levers) and several 100 kHz (noncontact levers). The torsion eigenfrequencies are usually one order of magnitude larger. For noncontact applications bare Si tips are commonly used.

5.4 Topographies

Much progress has been made in understanding atomistic properties of surfaces by noncontact AFM [216]. In noncontact mode true atomic resolution was first obtained on Si(111)7×7 [217], on InP(110) [218], and on NaCl [219]. Meanwhile, even subatomic features are observable by noncontact AFM [220]. In contact mode, atomic resolution is achievable but unlike with STM and noncontact AFM it is inconclusive if this resolution is real. True atomic resolution can be recognized by the correct imaging of lattice defects, for example, vacancies as depressions. Otherwise, apparent atomic resolution can arise from the corrugations of the tip's surface and the sample's surface being in phase. The image is then a superposition of many patches of the surface and vacancies cannot be seen.

The AFM is mostly used to image physical properties of biological samples and organic layers [194, 195]. There are a few examples with high-resolution topographs of organic layers [221, and references therein]. With softer materials of macromolecular size or biological cells resolution drops drastically, especially in liquids. Noncontact measurements are, in principle, nondestructive but the topographies can be influenced by long range forces and are not completely reliable.

The motivation for the study of topography and atomic structure is the relation of function to structure. Topography often is acquired as a control channel, simultaneously with other physical properties. In the following section we give a few examples.

5.5 Beyond Topography

When using frequency modulation detection of the force gradient, the amplitude is kept constant. The signal to compensate for the damping, which is necessary to maintain a constant amplitude, reflects the energy loss of the oscillation. A contrast in the damping image arises therefore at places where the oscillating system dissipates more or less energy. That is related to a local change in the quality factor of the oscillation. The damping image might be regarded as similar to the lateral force image in the contact mode (Section 5.3.6).

It was reported that on Au(111) the damping at steps especially close to dislocations is weaker compared to the terraces [214]. Furthermore, the damping lines were reported to deviate from the actual step lines. Rigid dislocations in the subsurface region, which might not necessarily be attached to steps, might explain these observations. On Si(111)7 × 7 the damping was found to be stronger at the steps than on terraces [214], resulting in bright step lines in the damping images.

Despite the general interpretation of damping as energy dissipation, the exact physical mechanisms are not yet fully understood. Damping might be attributed to local excitations of phonons or to tip-sample contacts at the reversal point near the surface. During contacts the chemical reactivity of the surface material will increase the damping. This effect can be modulated with topographical features because the size of the interaction area governs the extent of the chemical reactivity, for example, at steps the damping will in general be lowered.

Organic islands on a silicon substrate might serve as a good example of the difficulty of interpreting damping images [222]. The soft organic layer is decisively different from the relatively hard silicon substrate and one might expect a material specific contrast in the damping image. The noncontact topography in Figure 66b shows bright fractal-shaped islands of self assembled octadecyltrichlorosilane (OTS) molecules (Fig. 66a) on activated Si(111). The OTS was deposited by a Langmuir-Blodgett technique. As the assembling of larger OTS aggregates has already taken place in the solution the age of the solution is an important parameter and allows for control of size and density of the OTS islands.

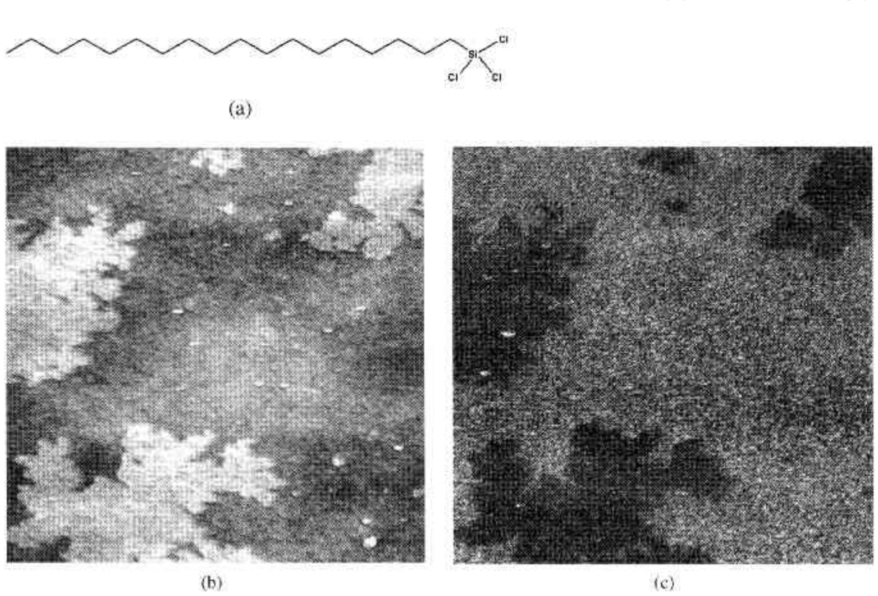

FIG. 66. Octadecyltrichlorosilane molecule (OTS, $C_{18}H_{37}Cl_3Si$) (length = 26 Å) (a) AFM noncontact topography image of self-assembled OTS film on Si_x/Si(111); 1.0 μm, $\Delta f = -54$ Hz (at 740 Hz), amplitude = 0.2 V. The apparent height of the islands is 16 Å, (b) Simultaneously acquired damping image (c). The Si surface was activated by UV/ozone treatment prior to exposure. The time of exposure was 20 s and the age of the OTS solution 10 min.

The simultaneously acquired damping map is shown in Figure 66c. Here, the fractal-shaped OTS islands appear dark, indicating less energy dissipation on the islands as compared to that on the silicon substrate. A possible explanation is the different chemical reactivity of the substrate and the OTS. The saturated hydrocarbon chains of the OTS do not react with the silicon tip as strongly as with the activated silicon substrate. Therefore, adhesion forces between tip and sample will be stronger on substrate regions than on OTS regions.

In magnetic force microscopy (MFM) [223, 224] the tip of the flexible cantilever is covered by a ferromagnetic material and magnetized prior to the measurement. The magnetic stray field of the sample leads to a force onto the magnetized tip. This is a long-range interaction and it can be detected up to several 10 nm away from the surface. The measurement is performed in noncontact mode, that is, the frequency shift is used as a feedback signal. With soft-magnetic tips magnetic domains and/or domain walls can be imaged, that is, of a track on a hard disk [225] and of Co dots [226]. The lateral resolution typically reached in MFM is approximately 50 nm. In case of a hard-magnetic tip and a soft magnetic sample it is possible to "write" magnetically with the AFM tip [227].

Analogously, in electrostatic force microscopy (EFM) electrostatic forces can be used in the regulation feedback [228, 229]. Ferroelectric media can be polarized by a voltage applied to a conductive AFM probe in contact (writing). The surface polarization leads to a long range force that can be detected via interaction with the probe at low bias. This interaction force is used as feedback in noncontact mode (reading).

Scanning Kelvin force microscopy (KFM) uses the tip-sample-contact as a local Kelvin probe and allows acquisition of contact potential (CP) distributions or work function maps with nanometer resolution. Initially, such experiments have been performed in atmosphere [230, 231]. Because the work function of most surfaces is altered by oxidation and adsorption, this method was augmented for measurements under UHV conditions [232]. The tip-sample contact represents a capacity that varies during the cantilever oscillation. Additionally, both ac and dc voltage are applied. The result is a time-varying electrostatic force that is minimal, when the dc voltage U_{dc} and the work function difference $\Delta\Phi/e$ compensate. During scanning the dc voltage is adjusted to the force minimum by a feedback loop and a CP map ($U_{\mathrm{dc}}(x, y)$) is acquired. This is similar to conventional (nonlocal) Kelvin probes where the current instead of the force is minimized.

5.6 Force Spectroscopy

In the spectroscopy mode of AFM force-distance curves $F(z)$ are recorded at one or more scan points after the z piezo has been adjusted to the force setpoint (contact mode). The classical shape, as illustrated in Section 5.3.4 and Figure 63, is obtained mostly with hard materials or simpler molecules. In air a meniscus of water is formed at the jump-to-contact. Due to the meniscus force the jump-to- and jump-off-contact separations differ largely and the area of the hysteresis loop becomes quite large. Force-distance curves can have various appearances. An overview is given in Reference [233]. Spectroscopy is rarely employed in the dynamic mode because with an oscillating probe the tip-sample separation is never well-defined. On the other hand the snap-on is avoided and the complete interaction potential can be inferred from the measured frequency versus distance curve employing simulations [234, 235].

When the tip is functionalized with a chemical species, chemical discrimination can be achieved (chemical force microscopy, CFM) [236, 237]. Covalently functionalized nanotubes can be prepared, allowing chemical contrast between areas with different SAM layers [238]. For biomolecular applications tips can be chemically modified by a layer of molecules that bind especially strongly to complementary molecules. Insight into mechanical properties of biomolecules, such as binding/recognition interactions, unfolding, and elasticity of complex biomolecules has been gained on the basis of force-distance curves [239–243].

6 COMPARATIVE CONSIDERATIONS

The different surface analytical methods are compared in Table V with respect to the method used, chemical information, structural information, sensitivity, probing depth and lateral resolution. The comparison is given in qualitative terms defining ranges rather than absolute limits. There are special instruments which surpass some of the specifications given. Some of the listings are physical limits, e.g., diffraction methods give long range structural information in principal, all local information is obtained by calculations based on models. All diffraction methods provide, however, the most accurate lattice constants. In contrast,

TABLE V. General Characteristics of Surface Analytical Methods

Method	Excitation detection	Information chemical	Information structural	Monolayer resolution	Effective probing depth	Lateral resolution
LEIS	Ion-ion	Elements Be–U	Short-range order	10^{-2}	<1 nm	1 μm^2
RBS	Ion-ion	Elements Be–U	Order via channeling	10–10^{-4}	10 nm	1 mm^2
SIMS	Ion-ion	Elements H–U	None	10^{-5}	1 nm	100 nm^2
LEED RHEED	Electron-electron	Poor	Long-range order	poor	1 nm	100 nm^2
AES	Electron-electron	Elements Li–U	None	10^{-2}	2 nm	100 nm^2
XPS	Photon-electron	Elements Li–U Chemical bonding	Short-range order via XPD	10^{-1}	3 nm	10 μm^2
STM	Tip-current	Poor	Short-range order	poor	<1 nm	0.1 nm^2
AFM	Tip-force	Poor	Short-range order	poor	<1 nm	0.1 nm^2

TABLE VI. Some Special Aspects of Surface Analytical Methods with Chemical Sensitivity

Features	LEIS	RBS	SIMS	SNMS	AES	XPS
Elements not directly detected	H, He	H, He	None	None	H, He	H, He
Detection of H and He	Via recoils	Via recoils ERDA	Direct	Direct	Via line shapes ESCA	High resolution
Isotope detection	Low Z	Low Z	Yes All masses	Yes All masses	No	No
Variation of detection with Z	~10^2	~10^3	10^4–10^5	10–10^2	~20	~20
Organic sample Polymers	Elements at the surface, poor	Elements in depth range	Total mass, fragments, elements	Total mass, fragments, elements	Elements, line shapes	Elements, chem. shifts, valence band
Damage	small	Very small	Yes	Yes	small	Very small
Charging	Yes	Small	Yes	Yes	Yes	Small
Quantification	Using elem. Standards	Complete	Very poor	Good	Using elem. standards	Yes
Deviation	5%	2%	5–100%	5–10%	1–5%	1%
Depth profiling	Via sputtering	Via energy loss	Sputtering	Sputtering	Via sputtering	Line shape analysis, sputtering

STM and AFM are local probes, long range information is limited by the scanning range and/or the management of adding up scanning areas, the final limit being the total scanning time with respect to the time stability of the sample. Table VI compares some aspects of the surface analytical methods providing chemical sensitivity. Again, the listings are rather qualitative. Completeness is not the goal of this representation, e.g., PIXE is not mentioned using proton excited X-rays for chemical analysis. All variations of photoelectron spectroscopy including ESCA (Electron Spectroscopy for Chemical Analysis) are summarized under the heading XPS. The features listed are in many discussions the key issues when decisions are to be made which instrument to chose for the problem at hand.

References

1. M. Schleberger, S. Speller, and W. Heiland, *Exp. Meth. in the Physical Sciences* 30, 291 (1998).
2. H. Niehus, W. Heiland, and E. Taglauer, *Surf. Sci. Rep.* 17, 213 (1993).
3. J. Lindhard, *Kong. Danske Vidensk. Selsk. Mat.-Fys. Medd.* 34, 1 (1965).
4. M. Hou and M. T. Robinson, *Appl. Phys.* 17, 371 (1978).
5. E. Rutherford, *Phil. Mag.* 21, 669 (1911).
6. G. Moliere, *Z. Naturforsch.* 2a, 133 (1947).
7. J. F. Ziegler, J. P. Biersack, and U. Littmark, "The Stopping and Range of Ions in Solids." Vol. 1. Pergamon Press, New York, 1985.
8. E. Taglauer, in "Surface Analysis—The Principal Techniques." J. C. Vickerman, Ed., John Wiley & Sons, Ltd., p. 215, 1997.
9. For example: H. Goldstein, "Classical Mechanics." Addison-Wesley, Reading, MA, 1965.
10. M. T. Robinson and I. M. Torrens, *Phys. Rev.* B9, 5008 (1974).
11. M. Hou and M. T. Robinson, *Appl. Phys.* 17, 317 (1978).
12. J. P. Biersack and L. G. Haggmark, *Nucl. Inst. Meth.* 174, 507 (1980).
13. J. P. Biersack and W. Eckstein, *Appl. Phys.* 34, 73 (1984).
14. W. Eckstein, "Computer Simulation of Ion-Solid Interactions." Springer-Verlag, Berlin, 1991.
15. W.-K. Chu, J. W. Mayer, and M.-A. Nicolet, "Backscattering Spectrometry." Academic Press, New York, 1978.
16. L. C. Feldman and J. W. Mayer, "Fundamentals of Surface and Thin Film Analysis." North Holland, Amsterdam, 1986.
17. H. H. Andersen, "The Stopping Power and Ranges of Ions in Matter." Pergamon Press, New York, 1977.
18. L. R. Doolittle, *Nucl. Instr. Meth. in Phys. Res.* B9, 344 (1985).
19. Z. L. Liau, J. W. Mayer, W. L. Brown, and J. M. Poate, *J. Appl. Phys.* 49, 5295 (1978).
20. J. F. van der Veen, B. Pluis, and A. W. Denier van der Gon, in "Kinetics of Ordering and Growth on Surfaces" (M. G. Lagally, Ed.), p. 34, Plenum Press, New York, 1990.
21. J. W. M. Frenken and J. F. van der Veen, *Phys. Rev. Lett.* 54, 134 (1985).

22. S. A. E. Johansson and J. L. Campbell, "Pixe—A Novel Technique For Elemental Analysis." John Wiley, New York, 1988.
23. M. Aschoff, Ph.D. Dissertation (Thesis), Osnabrück, 1999 (http://elib.Uni-Osnabrueck.DE/dissertations/physics/M.Aschoff/).
24. H. H. Brongersma and G. C. van Leerdam, in "Fundamental Aspects of Heterogeneous Catalysis Studied by Particle Beams" (H. H. Brongersma and R. A. van Santen, Eds.), NATO ASI Series B265, 283 (1991).
25. H. D. Hagstrum, in "Inelastic Ion—Surface Collisions" (N. H. Tolk, J. C. Tully, W. Heiland, and C. W. White, Eds.), p. 1, Academic Press, New York, 1977.
26. I. S. Tsong, in "Inelastic Particle—Surface Collisions" (E. Taglauer and W. Heiland, Eds.), p. 258, Springer, Heidelberg, 1981.
27. R. Hoekstra, J. Manske, M. Dirska, G. Lubinski, M. Schleberger, and A. Naermann, in "Inelastic Ion Surface Collisons." *Proc. of the IISC-11* (W. Heiland and E. Taglauer, Eds.), *Nucl. Instr. Meth.* B125, 53 (1997).
28. H. Brenten, H. Müller, and V. Kempter, *Phys. Rev. Lett.* 70, 25 (1993).
29. J. Los and J. J. C. Geerlings, *Rep. Progr. Phys.* 190, 133 (1990).
30. W. Heiland, in "Low Energy Ion-Surface Interactions" (J. W. Rabalais, Ed.), p. 313, John Wiley & Sons, New York, 1994.
31. E. C. Goldberg, R. Monreal, F. Flores, H. H. Brongersma, and P. Bauer, *Surf. Sci. Lett.* (1999).
32. R. L. Ericksen and D. P. Smith, *Phys. Rev. Lett.* 34, 297 (1975).
33. A. Zartner, E. Taglauer, and W. Heiland, *Phys. Rev. Lett.* 40, 1259 (1978).
34. J. C. Tully, *Phys. Rev.* B16, 4324 (1977).
35. E. Taglauer, W. Englert, W. Heiland, and D. P. Jackson, *Phys. Rev. Lett.* 45, 740 (1980).
36. D. P. Jackson, W. Heiland, and E. Taglauer, *Phys. Rev.* B24, 4198 (1981).
37. E. Taglauer, in "Ion Spectroscopies for Surface Analysis" (A. Czanderna and D. M. Hercules, Eds.), Plenum Publ. Co., New York, 1991.
38. H. H. Brongersma, M. Carriere-Fontaine, R. Cortenraad, A. W. Denier van der Gon, J. P. Scanlon, I. Spolveri, B. Cortigiani, U. Bardi, E. Taglauer, S. Reiter, S. Labich, P. Bertrand, L. Houssiau, S. Speller, S. Parascandola, H. Unlü-LAchnitt, and W. Heiland, *Nucl. Instr. Meth.* B142, 377 (1998).
39. J. Kuntze, S. Speller, W. Heiland, P. Deurinck, C. Creemers, A. Atrei, and U. Bardi, *Phys. Rev.* B60, 9010 (1999).
40. A. Niehof and W. Heiland, *Nucl. Instr. Meth.* B48, 306 (1990).
41. S. Speller, M. Schleberger, A. Niehof, and W. Heiland, *Phys. Rev. Lett.* 68, 3452 (1992).
42. Y. Fujii, K. Namuri, K. Kimura, M. Mannami, T. Hashimoto, K. Ogawa, F. Ohtani, T. Yoshida, and M. Asari, *Appl. Phys. Lett.* 63, 2070 (1993).
43. R. Pfandzelter, *Surf. Sci.* 421, 263 (1999).
44. M. Aono, C. Oshima, S. Zaima, S. Otani, and Y. Ishizawa, *Jap. J. Appl. Phys.* 20, L829 (1981).
45. H. Niehus, *Nucl. Instr. Meth.* 218, 230 (1983).
46. M. Aschoff, S. Speller, J. Kuntze, W. Heiland, E. Platzgummer, M. Schmid, P. Varga, and B. Baretzky, *Surf. Sci.* 415, L1051 (1998).

47. C. Kim, C. Hoefner, and J. W. Rabalais, *Surf. Sci. Lett.* 388, 11085 (1997).
48. C. Kim, C. Hoefner, V. Bykov, and J. W. Rabalais, *Nucl. Instr. Meth.* B125, 315 (1997).
49. C. Kim, J. Ahn, V. Bykov, and J. W. Rabalais, *Int. J. Mass Spectr. Ion Phys.* 174, 305 (1998).
50. C. Hoefner and J. W. Rabalais, *Phys. Rev.* B58, 9990 (1998).
51. Ch. Linsmeier, H. Knetzinger, and E. Taglauer, *Surf. Sci.* 275, 101 (1992).
52. A. W. van der Gon, R. Cortenraad, W. P. A. Jansen, M. A. Reijme, and H. H. Brongersma, *Nucl. Instr. Meth.* B161–163, 56 (2000).
53. L. Houssiau and J. W. Rabalais, *Nucl. Instr. Meth.* B157, 274 (1999).
54. P. Sigmund, *Phys. Rev.* 184, 383 (1969).
55. R. Behrisch (Ed.), "Sputtering by Particle Bombardment I and II." *Topics Appl. Phys.*, Springer, Berlin, 47 (1981); 52 (1983).
56. R. Behrisch and K. Wittmaack (Eds.), "Characteristics of Sputtered Particles Applications." *Topics Appl. Phys.*, Springer, Berlin, 64 (1991).
57. H. Oechsner, *J. Mass Spectr. Ion Proc.* 143, 271 (1995).
58. C. E. Young, M. J. Pellin, W. F. Callaway, B. Jørgensen, E. L. Schreiber, and D. M. Gruen, *Nucl. Instr. Meth.* B27, 119 (1987).
59. H. Gnaser, *J. Vac. Sci. Tech.* A12, 452 (1994).
60. H. Gnaser, *J. Vac. Sci. Tech.* A15, 445 (1997).
61. H. Oechsner, *J. Mass Spectrometry and Ion Proc.* 143, 271 (1995).
62. A. Benninghoven, F. G. Rüdenauer, and H. W. Werner, "Secondary Ion Mass Spectrometry." Wiley, New York, 1987.
63. www-hasylab.desy.de/science/groups/materlik-group/research.html B. N. Dev and G. Materlik, in "Resonant Anomalous X-ray Scattering" (G. Materlik, C. J. Sparks, and K. Fischer, Eds.), pp. 119–145, North Holland, Amsterdam, 1994.
64. H. Dosch, *Appl. Phys.* A61, 475 (1995).
65. J. Als-Nielsen, *Physica* A40, 376 (1986).
66. H. Dosch, "Critical Phenomena at Surfaces and Interfaces." *Springer Tracts in Modern Physics*, Springer, Heidelberg, 1995.
67. S. Krimmel, W. Donner, B. Nickel, and H. Dosch, *Phys. Rev. Lett.* 78, 3880 (1998).
68. W. Donner, H. Dosch, S. Ulrich, H. Ehrhardt, and D. Abernathy, *Appl. Phys. Lett.* 73, 777 (1998).
69. C. J. Davisson and L. H. Germer, *Phys. Rev.* 30, 705 (1927).
70. R. L. Park and H. E. Farnsworth, *Rev. Sci. Instr.* 35, 1592 (1964).
71. G. Scheithauer, G. Meyer, and M. Henzler, *Surf. Sci.* 178, 441 (1986).
72. M. Lagally, *Meth. in Exp. Phys.* 22, 237 (1985).
73. K. Heinz, *Rep. Progr. Phys.* 58, 637 (1995).
74. K. Heinz, M. Kottke, U. Löffler, and R. Döll, *Surf. Sci.* 357-358, 1 (1996).
75. www.fkp.uni-hannover.de/fkp/research/spaleed/spaleed.html
76. J. B. Pendry, "Low Energy Electron Diffraction." Academic Press, London, 1974.
77. M. A. Van Hove and S. Y. Tong, "Surface Crystallography by LEED." Springer, Berlin, 1979.
78. C. B. Duke, *Surf. Sci.* 299/300, 24 (1994).
79. J. B. Pendry, *Surf. Sci.* 299/300, 375 (1994).

80. J. M. MacLaren, J. B. Pendry, P. J. Rous, D. K. Saldin, G. A. Somorjai, M. A. Van Hove, and D. D. Vvedensky, "Surface Crystallographic Information Service." D. Reidel Publ. Co, Dordrecht, 1987; For new information see: http://www.nist.gov/srd/nist42.htm
81. A. Barbieri and M. A. Van Hove, Symmetrized Automated Tensor LEED Package, Version 4.1, Private communication (1999).
82. A. Barbieri and A. M. Van Hove, Private communication (1999).
83. S. Crampin and P. J. Rous, *Surf. Sci. Lett.* 244, L137 (1991).
84. J. Pendry, *J. Phys.* C13, 937 (1980).
85. A. M. Van Hove, W. H. Weinberg, and C.-M. Chan, "Low Energy Electron Diffraction" (G. Ertl and R. Gomer, Eds.), *Springer Series in Surface Science*, 6, Springer Verlag, Berlin, 1986.
86. A. Zangwill, "Physics at Surfaces." Cambridge University Press, Cambridge, 1988.
87. www.fkp.uni-erlangen.de/fkp/literatur/pubholo.html
88. P. K. Larson and P. J. Dobson, "Reflection High Energy Electron Diffraction." *NATO ASI Series*, 188, Plenum Press, New York, 1988.
89. M. Hoheisel, J. Kuntze, S. Speller, A. Postnikov, and W. Heiland, *Phys. Rev.* B60, 2033 (1999).
90. A. N. Haner, P. N. Ross, and U. Bardi, *Surf. Sci.* 249, 15 (1991).
91. J. Kunze, S. Speller, W. Heiland, A. Atrei, I. Spolveri, and U. Bardi, *Phys. Rev.* B58, R16005 (1998).
92. M. Hoheisel, S. Speller, J. Kuntze, U. Bardi, and W. Heiland, *Phys. Rev.* B (2001).
93. G. A. Prinz, *Physics Today* April, 58 (1995).
94. G. Bayreuther and S. Mengel, "Magnetoelektronik, Grundlagenforschung—Zukunftstechnologie?" VDI-Technologiezentrum, 1998.
95. P. Walser, M. Schleberger, P. Fuchs, and M. Landolt, *Phys. Rev. Lett.* B80, 2217 (1998).
96. M. Schleberger, P. Walser, M. Hunziker, and M. Landolt, *Phys. Rev.* B60, 14360 (1999).
97. E. Bauer, *Z. Kristallogr.* 110, 372 (1958).
98. D. A. Shirley, *Phys. Rev.* B5, 4709 (1972).
99. S. Tougaard and C. Jansson, *Surf. Interface Anal.* 20, 1013 (1993).
100. S. Tougaard and P. Sigmund, *Phys. Rev.* B25, 4452 (1981).
101. S. Tougaard, *Surf. Interface Anal.* 11, 453 (1988).
102. S. Tougaard, *J. Vac. Sci. Technol.* 8, 2198 (1990).
103. M. P. Seah and W. A. Dench, *Surf. Interface Anal.* 1, 2 (1979).
104. S. Tanuma, C. J. Powell, and D. R. Penn, *Surf. Interf. Anal.* 11, 577 (1988).
105. J. Lindhard, *K. Dan. Vidensk. Selsk. Mat.-Fys. Medd.* 28, 1 (1954).
106. R. Ritchie and A. Howie, *Philos. Mag.* 36, 463 (1977).
107. S. Tougaard and I. Chorkendorff, *Phys. Rev.* B 35, 6570 (1987).
108. S. Tougaard and J. Kraaer, *Phys. Rev.* B 43, 1651 (1991).
109. S. Tougaard, *Solid State Commun.* 61, 547 (1987).
110. S. Tougaard, *Surf. Interface Anal.* 25, 137 (1997).
111. M. Schleberger, *Surf. Sci.* 445, 71 (2000).
112. M. Schleberger, D. Fujita, C. Scharfschwerdt, and S. Tougaard, *Surf. Sci.* 331-333, 942 (1995).

113. M. Schleberger, D. Fujita, and S. Tougaard, *J. Electr. Spectr.* 82, 173 (1996).
114. E. N. Sickafus, *Phys. Rev.* B 16, 1436 (1977).
115. M. Gryzinski, *Phys. Rev. A* 138, 336 (1965).
116. M. Schleberger, D. Fujita, C. Scharfschwerdt, and S. Tougaard, *J. Vac. Sci. Technol.* B13, 949 (1995).
117. E. Daugy, P. Mathiez, F. Salvan, and J. Layet, *Surf. Sci.* 154, 267 (1985).
118. T. Yasue, T. Koshikawa, H. Tanaka, and I. Sumita, *Surf. Sci.* 287/288, 1025 (1993).
119. P. Ho, G. W. Rudloff, J. E. Lewis, V. L. Moruzzi, and A. R. Williams, *Phys. Rev.* B22, 4784 (1980).
120. R. Matz, R. J. Purtell, Y. Yakota, G. W. Rudloff, and P. S. Ho, *J. Vac. Sci. Technol.* A2, 253 (1984).
121. R. Kern, G. L. Lay, and M. Manville, *Surf. Sci.* 72, 405 (1978).
122. G. L. Lay, *Surf. Sci.* 132, 169 (1983).
123. S. Ino and A. Endo, *Surf. Sci.* 293, 165 (1993).
124. K. Sumitomo, T. Kobayashi, F. Shoji, K. Oura, and I. Katayama, *Phys. Rev. Lett.* 66, 1193 (1991).
125. J.-J. Yeh, J. Hwang, K. Bertness, D. J. Friedman, R. Cao, and I. Lindau, *Phys. Rev. Lett.* 70, 3768 (1993).
126. A. Cros, J. Derrien, F. Salvan, and J. Gaspard, *Proc. ECOSS-3*, unpublished (1980).
127. M. Schleberger, A. Cohen Simonsen, S. Tougaard, J. L. Hansen, and A. N. Nylandsted, *J. Vac. Sci. Techn.* A15, 3032 (1997).
128. A. Cohen Simonsen, M. Schleberger, S. Tougaard, J. L. Hansen, and A. N. Nylandsted Larsen, *Thin Solid Films* 338, 165 (1999).
129. Y. W. Mo, D. Savage, B. Schwarzentruber, and M. Lagally, *Phys. Rev. Lett.* 65, 1020 (1990).
130. M. Asai, H. Ueba, and C. Tatsuyama, *J. Appl. Phys.* 58, 2577 (1985).
131. E. Richmond, *Thin Solid Films* 252, 98 (1994).
132. P. Grütter, W. Zimmermann-Edling, and D. Brodbeck, *Appl. Phys. Lett.* 60, 2741 (1992).
133. S. Sheiko, M. Möller, E. Reuvekamp, and H. Zandbergen, *Phys. Rev.* B48, 5675 (1993).
134. S. S. P. Parkin, N. More, and K. P. Roche, *Phys. Rev. Lett.* 64, 2304 (1990).
135. P. Grünberg, R. Schreiber, Y. Pang, M. B. Brodsky, and H. Sowers, *Phys. Rev. Lett.* 57, 2442 (1986).
136. P. Zahn, I. Mertig, M. Richter, and H. Eschrig, *Phys. Rev. Lett.* 75, 2996 (1995).
137. S. Toscano, B. Briner, H. Hopster, and M. Landolt, *Phys. Rev. Lett.* 73, 340 (1994).
138. R. Kilper, St. Teichert, Th. Franke, P. Häussler, H. G. Boyen, A. Cossy-Favre, and P. Oelhafen, *Appl. Surf. Sci.* 91, 93 (1995).
139. P. Häussler, Private communication.
140. J. J. de Vries, J. Kohlhepp, F. J. A. den Broeder, R. Coehoorn, R. Jungblut, A. Reinders, and W. J. M. de Jonge, *Phys. Rev. Lett.* 78, 3023 (1997).
141. C. Dufour, A. Bruson, G. Marchal, B. George, and Ph. Magnin, *J. Magn. Magn. Mat.* 93, 545 (1991).
142. G. Binnig, H. Rohrer, C. Gerber, and H. Weibel, *Phys. Rev. Lett.* 50, 120 (1993)

143. Absolute distance measure is not directly possible, as the nanoscopic tip shape is unknown in general. However, the distance can be measured by the z piezovoltage necessary to drive the tip into a soft crash with the sample.
144. W. Moritz and D. Wolf, *Surf. Sci.* 88, L29 (1979); 163, L655 (1985).
145. G. Binnig, H. Rohrer, C. Gerber, and H. Weibel, *Surf. Sci.* 131, L379 (1983).
146. H. P. Bonzel and R. Ku, *Sci. Technol.* 9, 633 (1972).
147. T. Gritsch, D. Coulman, R. J. Behm, and G. Ertl, *Phys. Rev. Lett.* 63, 1086 (1998); *Surf. Sci.* 257, 297 (1991).
148. J. K. Gimzewski, R. Berndt, and R. R. Schlittler, *Surf. Sci.* 247, 327 (1997); *Phys. Rev.* B 45, 6844 (1992).
149. A. Zangwill, "Physics at Surfaces." Cambridge University Press, Cambridge, 1988.
150. S. Speller, J. Kuntze, T. Rauch, J. Bömermann, M. Huck, M. Aschoff, and W. Heiland, *Surf. Sci.* 366, 251 (1996).
151. R. Koch, M. Borbonus, O. Haase, and K. H. Rieder, *Phys. Rev. Lett.* 67, 3416 (1991).
152. J. Kuntze, The Atomic Structure of the Clean and Adsorbate Covered Ir(110) Surface, Ph.D. Dissertation (Thesis) (1999). (http://elib.Uni-Osnabrueck.DE/dissertations/physics/J.Kuntze/thesis.ps.gz).
153. J. J. Schulz, M. Sturmat, and R. Koch, *Phys. Rev.* B 62, 15402 (2000).
154. P. Hanesch and E. Bertel, *Phys. Rev. Lett.* 79, 1523 (1997).
155. E. D. Williams, *Surf. Sci.* 299/300, 502 (1994).
156. C. Alfonso, J. M. Bermond, J. C. Heyraud, and J. J. Metois, *Surf. Sci.* 262, 371 (1992).
157. M. Giesen, *Surf. Sci.* 370, 55 (1997).
158. L. Barbier, L. Masson, J. Cousty, and B. Salanon, *Surf. Sci.* 345, 197 (1996).
159. J. W. M. Frenken and P. Stoltze, *Phys. Rev. Lett.* 82, 3500 (1999).
160. R. Smoluchowski, *Phys. Rev.* 60, 661 (1941).
161. R. Stumpf and M. Scheffler, *Phys. Rev.* B 53, 4958 (1996).
162. H.-C. Jeong and E. D. Williams, *Surf. Sci. Rep.* 34, 171 (1999).
163. A. Bachmann *et al.*, to be published.
164. A. R. Bachmann, A. Mugarza, J. E. Ortega, A. Närmann, and S. Speller, to be published.
165. M. Giesen, *Prog. Surf. Sci.*, in press (2001).
166. A. V. Ruban, H. I. Skriver, and J. K. Norskov, *Phys. Rev.* B 59, 15990 (1999).
167. B. M. Ocko, D. Gibbs, K. G. Huang, D. M. Zehner, and S. G. J. Mochrie, *Phys. Rev.* B 44, 6429 (1991).
168. L. Bönig, S. Liu, and H. Metiu, *Surf. Sci.* 365, 87 (1991).
169. J. Kuntze, S. Speller, W. Heiland, A. Atrei, G. Rovida, and U. Bardi, *Phys. Rev.* B 60, 1535 (1999).
170. U. Bardi, L. Pedocchi, G. Rovida, A. N. Haner, and P. N. Ross, in "Fundamental Aspects of Heterogenous Catalysis Studied by Particle Beams" (H. H. Brongersma and R. A. van Sannen, Eds.), p. 393, Plenum Press, New York, 1991.
171. A. Atrei, U. Bardi, G. Rovida, M. Torrini, E. Zanazzi, and P. N. Ross, *Phys. Rev.* B 46, 1649 (1992).
172. L. Vitos, A. V. Ruban, H. L. Skriver, and J. Kollár, *Surf. Sci.* 411, 186 (1998).
173. M. Schmid, H. Stadler, and P. Varga, *Phys. Rev. Lett.* 70, 1441 (1993).

174. H. Brune, *Surf. Sci. Rep.* 31, 121 (1998).
175. S. Speller, S. Degroote, J. Dekoster, G. Langouche, J. E. Ortega, and A. Närmann, unpublished.
176. J. de la Figuera, J. E. Prieto, C. Ocal, and R. Miranda, *Surf. Sci.* 307–309, 538 (1994).
177. J. de la Figuera, J. E. Prieto, G. Koska, S. Müller, C. Ocal, R. Miranda, and K. Heinz, *Surf. Sci.* 349, L139 (1996).
178. M. Klaua, H. Höche, H. Jenniches, J. Barthel, and J. Kirschner, *Surf. Sci.* 381, 106 (1997).
179. S. Speller, S. Degroote, J. Dekoster, G. Langouche, J. E. Ortega, and A. Närmann, *Surf. Sci. Lett.* 405, 542 (1998).
180. S. Morin, A. Lachenwitzer, O. M. Magnussen, and R. J. Behm, *Phys. Rev. Lett.* 83, 5066 (1999).
181. F. J. Himpsel, J. E. Ortega, G. J. Mankey, and R. F. Willis, *Adv. in Phys.* 47, 511 (1998).
182. G. Witte, J. Braun, D. Nowack, L. Bartels, B. Neu, and G. Meyer, *Phys. Rev.* B 58, 13224 (1998).
183. A. R. Bachmann, A. Mugarza, J. E. Ortega, A. Närmann, and S. Speller, in preparation.
184. F. Nouvertné, U. May, M. Bamming, A. Rampe, U. Korte, G. Güntherodt, R. Pentcheva, and M. Scheffler, *Phys. Rev.* B 60, 14382 (1999).
185. G. Ertl and H. J. Freund, *Physics Today*, Jan. 32 (1999).
186. J. Wintterlin, S. Völkening, T. V. W. Janssens, T. Zambelli, and G. Ertl, *Science* 278, 1931 (1997).
187. F. Besenbacher, I. Chorkendorff, B. S. Clausen, B. Hammer, A. M. Molenbroek, J. K. Nørskov, and I. Stensgaard, *Science* 279, 1913 (1998).
188. M. Hoheisel *et al.*, to be published.
189. I. S. Tilinin, M. K. Rose, J. C. Dunphy, M. Salmeron, and M. A. van Hove, *Surf. Sci.* 418, 511 (1998).
190. J. Bömermann, M. Huck, J. Kuntze, T. Rauch, S. Speller, and W. Heiland, *Surf. Sci.* 357/358, 849 (1996).
191. S. Speller, T. Rauch, J. Bömermann, P. Borrmann, and W. Heiland, *Surf. Sci.* 441, 107 (1999).
192. J. R. Sheats, H. Antoniadis, M. Hueschen, W. Leonard, J. Miller, R. Moon, D. Roitman, and A. Stocking, *Science* 273, 884 (1996).
193. Z. Shen, P. E. Burrows, V. Bulovi, S. R. Forrest, and M. E. Thompson, *Nature* 276, 2009 (1997).
194. A. Ikai, *Surf. Sci. Rep.* 26, 261 (1997).
195. J. A. DeRose and R. M. Leblanc, *Surf. Sci. Rep.* 22, 73 (1995).
196. http://www.zyvex.com/nanotech/feynman.html
197. D. D. Chambliss, R. J. Wilson, and S. Chiang, *Phys. Rev. Lett.* 66, 1721 (1991).
198. H. Brune, M. Giovannini, K. Bromann, and K. Kern, *Nature* 394, 451 (1998).
199. T. A. Jung, R. Schittler, J. K. Gimzewski, and F. J. Himpsel, *Appl. Phys.* A 61, 467 (1995).
200. J. E. Ortega, S. Speller, A. R. Bachmann, A. Mascaraque, E. Cr. Michel, A. Närmann, A. Mugarza, A. Rubic, and F. J. Himpsel, *Phys. Rev. Lett.* 84, 6110 (2000).

201. Th. Schulze, B. Berger, R. Mertens, M. Pivk, T. Pfau, and J. Mlynek, *Appl. Phys.* B 70, 671 (2000).

202. U. Drodofsky, J. Stuhler, Th. Schulze, M. Drewsen, B. Brezger, T. Pfau, and J. Mlynek, *Appl. Phys.* B 65, 755 (1997).

203. M. F. Crommie, C. P. Lutz, and D. M. Eigler, *Science* 262, 218 (1993).

204. H. C. Manoharan, C. P. Lutz, and D. M. Eigler, *Nature* 403, 512 (2000).

205. J. Li, W.-D. Schneider, R. Berndt, and S. Crampin, *Phys. Rev. Lett.* 80, 3332 (1998).

206. J. F. Jia, K. Inoue, Y. Hasegawa, W. S. Yang, and T. Sakurai, *Phys. Rev.* B 58, 1193 (1998).

207. G. Hörmandinger, *Phys. Rev.* B 49, 13897 (1994).

208. J. A. Stroscio and R. M. Feenstra, in "Scanning Tunneling Microscopy" (J. A. Stroscio and W. J. Kaiser, Eds.), Academic Press, New York, 1993.

209. S. Speller, T. Rauch, A. Postnikov, and W. Heiland, *Phys. Rev.* B 61, 7297 (2000).

210. B. C. Stipe, M. A. Rezaei, and W. Ho, *Science* 280, 1732 (1998); *Phys. Rev. Lett.* 82, 1724 (1999).

211. R. C. Jaklevic and J. Lambe, *Phys. Rev. Lett.* 17, 1139 (1966).

212. G. Binnig, C. F. Quate, and C. Gerber, *Phys. Rev. Lett.* 56, 930 (1986).

213. P. Vettiger, M. Despont, U. Drechsler, U. Dürig, W. Häberle, M. I. Lutwyche, H. E. Rothuizen, R. Stutz, R. Widmer, and G. K. Binnig, *IBM J. Res. Develop.* 44, 323 (2000).

214. S. Molitor, Ph.D. Dissertation (Thesis), Osnabrück; http://elib.Uni-Osnabrueck.DE/dissertations/physics/

215. H. Hölscher, U. D. Schwarz, O. Zwörner, and R. Wiesendanger, *Phys. Rev.* B 57, 2477 (1998).

216. "Proceedings of the Second International Workshop on Noncontact Atomic Force Microscopy" (R. Benewitz, Ed.), *Appl. Surf. Sci.* 157 (2000).

217. F. J. Giessibl, *Science* 267, 68 (1995).

218. Y. Sugawara, M. Ohta, H. Ueyama, and S. Morit, *Science* 270, 1646 (1995).

219. M. Bammerlin, R. Lüthi, E. Meyer, A. Baratoff, J. Lü, M. Guggisberg, Ch. Gerber, L. Howald, and H.-J. Güntherodt, *Probe Microscopy* 1, 3 (1997); or http://monet.unibas.ch/gue/uhvafm/pub_mb/nacl_pm.html

220. F. J. Giessibl, S. Hembacher, H. Bielefeldt, and J. Mannhart, *Science* 289, 422 (2000).

221. T. Uchihashi, T. Ishida, M. Komiyama, M. Ashino, Y. Sugawara, W. Mizutani, K. Yokoyama, S. Morita, H. Tokumoto, and M. Ishikawa, *Appl. Surf. Sci.* 157, 244 (2000).

222. M. Reiniger, B. Basnar, G. Friedbacher, and M. Schleberger, *Surface Interface Analysis*, accepted.

223. P. Grütter, H. J. Mamin, and D. Rugar, in "Scanning Tunneling Microscopy II" (R. Wiesendanger and H.-J. Günterodt, Eds.), Springer Verlag, Berlin Heidelberg, 1995.

224. Y. Martin and H. K. Wickramasinghe, *Appl. Phys. Lett.* 50, 1455 (1987).

225. T. D. Howell, D. P. McCown, T. A. Diola, and Y. S. Tang, *IEEE Trans. Magn.* 26, 2298 (1990).

226. M. Hehn, K. Ounadjela, J.-P. Bucher, F. Rousseaux, D. Decanini, B. Bartenlian, and C. Cahppert, *Nature* 272, 1782 (1996).

227. A. Born and R. Wiesendanger, *Appl. Phys.* A 68, 131 (1999).

228. R. Lüthi, H. Haefke, K.-P. Meyer, E. Meyer, L. Howald, and H.-J. Güntherodt, *J. Appl. Phys.* 74, 7471 (1993).

229. L. Eng, M. Bammerlin, C. Loppacher, M. Guggisberg, R. Bennewitz, R. Lüthi, E. Meyer, Th. Huser, H. Heinzelmann, and H.-J. Güntherodt, *Ferroelectrics* 222, 153 (1999).

230. M. Nonnenmacher, M. P. O'Boyle, and H. K. Wickramasinge, *Appl. Phys. Lett.* 58, 2921 (1991).

231. J. M. R. Weaver and D. W. Abraham, *J. Vac. Sci. Technol.* B 9, 1559 (1991).

232. S. Kitamura and M. Iwatsuki, *Appl. Phys. Lett.* 72, 3154 (1998).

233. B. Capella and G. Dietler, *Surf. Sci. Rep.* 34, 1 (1999).

234. H. Hölscher, W. Allens, U. D. Schwarz, A. Schwarz, and R. Wiesendanger, *Phys. Rev. Lett.* 83, 4780 (1999).

235. B. Gotsmann, B. Anczykowski, C. Seidel, and H. Fuchs, *Appl. Surf. Sci.* 140, 314 (1999).

236. C. D. Frisbie, L. F. Rozsnyai, A. Noy, M. S. Wrighton, and C. M. Lieber, *Science* 265, 2071 (1994).

237. A. Noy, D. V. Vezenov, and C. M. Lieber, *Annual Reviews of Materials Science* 27, 381 (1997).

238. S. S. Wong, E. Joselevich, A. T. Woolley, C. L. Cheung, and C. M. Lieber, *Nature* 394, 52 (1998).

239. M. Radmacher, *Physics World* 12, 33 (1999).

240. M. Rief, F. Oesterhelt, B. Heymann, and H. E. Gaub, *Science* 275, 1295 (1997).

241. M. Rief, M. Gautel, F. Oesterhelt, J. M. Fernandez, and H. E. Gaub, *Science* 276, 1109 (1997).

242. F. Oesterhelt, D. Oesterhelt, M. Pfeiffer, A. Engel, H. E. Gaub, and D. J. Müller, *Science* 288, 143 (2000).

243. H. Li, M. Rief, E. Oesterhelt, and H. E. Gaub, *Appl. Phys.* A 68, 407 (1999).

244. D. Fujita, M. Schleberger, and S. Tougaard, *Surf. Sci.* 357, 180 (1996).